Draft version October 27, 2010
Preprint typeset using LaTeX style emulateapj v. 03/07/07



# THE 1.6 MICRON NEAR INFRARED NUCLEI OF 3C RADIO GALAXIES: JETS, THERMAL EMISSION OR SCATTERED LIGHT?*

Ranieri D. Baldi[1,2], Marco Chiaberge[2,3], Alessandro Capetti[4], William Sparks[2], F. Duccio Macchetto[2], Christopher P. O'Dea[5], David J. Axon[5], Stefi A. Baum[5], and Alice C. Quillen[6]

*Draft version October 27, 2010*

## ABSTRACT

Using HST NICMOS 2 observations we have measured 1.6 $\mu$m near infrared nuclear luminosities of 100 3CR radio galaxies with z < 0.3, by modeling and subtracting the extended emission from the host galaxy. We performed a multi-wavelength statistical analysis (including optical and radio data) of the properties of the nuclei following classification of the objects into FR I and FR II, and LIG (low-ionization galaxies), HIG (high-ionization galaxies) and BLO (broad-lined objects) using the radio morphology and optical spectra, respectively. The correlations among near infrared, optical, and radio nuclear luminosity support the idea that the near infrared nuclear emission of FR Is has a non-thermal origin. Despite the difference in radio morphology, the multi-wavelength properties of FR II LIG nuclei are statistically indistinguishable from those of FR Is, an indication of a common structure of the central engine. All BLOs show an unresolved near infrared nucleus and a large near infrared excess with respect to FR II LIGs and FR Is of equal radio core luminosity. This requires the presence of an additional (and dominant) component other than the non-thermal light. Considering the shape of their spectral energy distribution, we ascribe the origin of their near infrared light to hot circumnuclear dust. A near infrared excess is also found in HIGs, but their nuclei are substantially fainter than those of BLO. This result indicates that substantial obscuration along the line-of-sight to the nuclei is still present at 1.6 $\mu$m. Nonetheless, HIGs nuclei cannot simply be explained in terms of dust obscuration: a significant contribution from light reflected in a circumnuclear scattering region is needed to account for their multiwavelength properties.

*Subject headings:* Galaxies: active – Galaxies: elliptical and lenticular, cD – Galaxies: nuclei – Galaxies: evolution – Galaxies: photometry – Galaxies: structure – Infrared: galaxies

## 1. INTRODUCTION

Infrared observations of radio galaxies are a useful tool to explore the physics of their nuclei in the framework of the Unified Models for Active Galactic Nuclei (AGN) as in this band the impact of dust absorption is strongly reduced with respect to the optical. In particular, the study of the infrared nuclear sources allows us to investigate the 'scheme' unifying different classes of AGN, by exploring the properties of their accretion disks and the presence of any absorbing material that can account for the complex AGN taxonomy.

In the "zeroth-order approximation" of the AGN unification scheme for radio-loud sources (e.g. Urry & Padovani 1995), powerful radio galaxies with FR II edge-brightened morphology (Fanaroff & Riley 1974) are believed to be misaligned quasars, while lower power, edge-darkened FR Is are associated with BL Lac objects. However, it is clear that this zeroth order approximation picture based on statistical comparison of the properties of radio-loud AGN is over-simplified. Inconsistencies between the characteristics of the "parent" and "beamed" populations are well reported in the literature: for example, several BL Lacs show broad emission lines (e.g. Vermeulen et al. 1995); and there are inconsistent environments (e.g. Zirbel 1997; Owen et al. 1996) and inconsistent radio morphologies (e.g. Antonucci 1986) (see also Urry & Padovani 1995 and Chiaberge 2004 for reviews on this subject).

Furthermore, how the large-scale radio properties relate to different nuclear properties is still not clear. In fact, there is mixed evidence for a correlation between the morphological FR I/FR II dichotomy and different levels of nuclear activity (Baum et al. 1995; Chiaberge et al. 1999; Xu et al. 1999a; Chiaberge et al. 2002a; Verdoes Kleijn et al. 2002). Another classification, based on the optical narrow emission lines ratios (Hine & Longair 1979; Laing et al. 1994; Jackson & Rawlings 1997; Buttiglione et al. 2010) introduces two groups of radio-loud AGN: the Low Excitation Galaxies (LEG) and High Excitation Galaxies (HEG)[7]. Radio galaxies with FR I radio morphology almost always belong to LEG class, while nearly all

* Based on observations made with the NASA/ESA Hubble Space Telescope, obtained at the Space Telescope Science Institute, which is operated by the Association of Universities for Research in Astronomy, Inc..
Electronic address: baldi@oato.inaf.it
[1] Universitá di Torino, via P. Giuria 1, I-10125 Torino, Italy; baldi@oato.inaf.it
[2] Space Telescope Science Institute, 3700 San Martin Drive, Baltimore, Baltimore, MD 21218
[3] INAF-Istituto di Radio Astronomia, via P. Gobetti 101, I-40129 Bologna, Italy
[4] INAF-Osservatorio Astronomico di Torino, Strada Osservatorio 20, 10025 Pino Torinese, Italy
[5] Department of Physics, Rochester Institute of Technology, Carlson Center for Imaging Science 76-3144, 84 Lomb Memorial Dr., Rochester, NY 14623, USA
[6] Department of Physics and Astronomy, University of Rochester, Rochester, NY 14627, USA

[7] In the following we will refer to those objects as High Ionization Galaxies (HIG) and Low Ionization Galaxies (LIG). See Sect. 2 for details.

HEGs are FR II radio sources. However, there is a group of FR II LEGs whose place in the unifying scenario is still largely not understood. Wall & Jackson (1997) and Jackson & Wall (1999) proposed that such objects constitute a single population of radio galaxies together with FR Is. In line with this idea, the two spectroscopic classes, LEG and HEG, show significant differences in several properties: star formation (e.g. Baldi & Capetti 2008; Smolčić 2009), environment (e.g. Chiaberge et al. 2000a; Hardcastle 2004), triggering mechanism of nuclear activity (gas-rich or gas-poor merger) (e.g. Baldi & Capetti 2008); there are indications that they differ also in terms of accretion rate and radiative efficiency of disk (e.g. Marchesini et al. 2004; Balmaverde et al. 2008); contrarily to what is seen in HEG, LEG do not show evidence for large absorbing column densities in the X-ray spectra (e.g. Hardcastle et al. 2006), for warm dusty tori in mid-IR images (van der Wolk et al. 2009), and for broad lines in their optical spectra (e.g. Buttiglione et al. 2010). Taken together these differences suggest that high and low excitation galaxies belong to different classes of radio-loud nuclear activity which are associated with distinct environmental conditions. Furthermore, it has been suggested that in the framework of the unification model, HEG and LEG might represent the parent population of QSOs and BL Lacs respectively (e.g. Jackson & Wall 1999).

A number of recent papers in the literature address the topic of the infrared view of the active nucleus of radio galaxies. Dicken et al. (2009) show that the infrared emission at both 24 and 70 micron can be explained in terms of dust heated predominantly by the AGN. More comprehensive mid-IR and far-IR spectrophotometry for the z < 1 3CR objects has been obtained from ISO (Siebenmorgen et al. 2004; Haas et al. 2004) as well as from Spitzer (e.g., Shi et al. 2005; Haas et al. 2005; Ogle et al. 2006; Cleary et al. 2007; Leipski et al. 2009). For high-redshift 3CR sources near infrared spectrophotometry using Spitzer has been presented by Haas et al. (2008) and Netzer et al. (2004).

The mid-infrared observations are sensitive to thermal emission from warm dust and have revealed rather complex properties within the different radio-galaxy classifications. The majority of FRIs are faint at those wavelengths, implying that the bulk kinetic power of the radio jets is the energetically dominant mechanism in most of these sources (Whysong & Antonucci 2004). Even in FR Is this is not a universal conclusion as Haas et al. (2004) with ISO data and Leipski et al. (2009) with Spitzer data show that in some FR Is a dust emission bump is detected. On the other hand, Ogle et al. (2006) found that about 50% of the FR II narrow-line radio galaxies have mid-infrared photometric and spectroscopic properties comparable to quasars of matched radio luminosity, while there is a subsample of mid-IR weak FR II radio galaxies which may constitute a separate population of non-thermal, jet-dominated sources with low accretion power. Haas et al. (2004) present evidence that the MIR data do in fact support the orientation-dependent unification scheme of the powerful FR II galaxies with quasars. This has been subsequently confirmed by further work, e.g. Haas et al. (2008); Ogle et al. (2006); Dicken et al. (2009).

This paper has the aim of investigating AGN activity by focusing on the nuclear 1.6 $\mu$m near infrared emission, identifying its physical origin and relating it to both the radio morphological and optical spectroscopic classes. Chiaberge et al. (1999, 2002a) studied the HST optical images of the nuclear regions of radio galaxies belonging to 3CR sample with the same purpose. The NIR snapshot survey of 3CR objects with $z < 0.3$ provided us with a larger coverage of the sample than that in the optical band. Furthermore, the fraction of 3CR sources with spectroscopic classification is now substantially larger (Buttiglione et al. 2010), allowing us to explore in greater detail the behavior of the nuclei of each class.

The resolution of HST images is suitable for this purpose and allow us to distinguish the NIR emission of stellar host galaxy background from the genuine AGN radiation.

The structure of the paper is as follows. In Sect. 2 we describe the sample and in Sect. 3 we derive the surface brightness profiles which we fit with either Sérsic or core-Sérsic models. The multiwavelength properties of our sample are discussed in Sect. 4 in order to identify the origin of the NIR nuclear emission tackled in Sect. 5. In Sect. 6 we summarize and draw conclusions. In Appendix we compare the FR I radio core flux observed with VLA and VLBI.

We adopt a Hubble constant of $H_0 = 75$ km s$^{-1}$ Mpc$^{-1}$ and $q_0 = 0.5$. We used this cosmology in order to be in accordance with the similar results obtained by Chiaberge et al. (1999), Chiaberge et al. (2000a), Chiaberge et al. (2002a). Assuming a different cosmology would not affect our results since the redshift of the sources considered in this paper is limited to $z = 0.3$.

## 2. SAMPLE AND HST OBSERVATIONS

The sample of galaxies we analyzed belongs to the Revised Third Cambridge Catalog 3CR (Bennett 1962b, Bennett 1962a, Spinrad et al. 1985). Since it is selected based on the low-frequency radio flux ($S_{178MHz} > 10$ Jy), the sample is essentially free from orientation bias. We chose all 116 3CR sources with z < 0.3 with the primary goal of characterizing the radio galaxy hosts mostly free from the effects of dust. One hundred objects were observed as part of HST/NICMOS 3CR snapshot program GO 10173 (PI: Sparks). The NIR images are published in Madrid et al. (2006) and Floyd et al. (2008). Only eleven galaxies were observed as a part of other programs and details of these are given in Table 1. We also included in the sample the FR I radio galaxy NGC 6251 because, as pointed out by Waggett et al. (1977) it should be included in 3CR catalog.

All of the objects of our sample were observed with HST NICMOS Camera 2 (NIC2), which has a field of view of $19\farcs2 \times 19\farcs2$ and a projected pixel size of $0.075''$, using the F160W filter (similar to H band), which is centered at 1.60 $\mu$m, covering a wavelength range from 1.4 to 1.8 $\mu$m and which includes the Pa$\beta$ line for objects with z > 0.1. Using the broad and narrow line H$\alpha$ fluxes measured for 3CR galaxies (Buttiglione et al. 2009) over a $2'' \times 2''$ aperture, we have estimate the contamination from line emission in the H band. In the case of the narrow lines we assumed ratio Pa$\beta$/H$\alpha$ = 0.06 from atomic physics (Osterbrock 1989). Since the broad line galax-

TABLE 1
Log of observations

| Name | Date yy-mm-dd | $t_{exp}$ s |
|---|---|---|
| 3C 084 | 1998-03-16 | 639.9 |
| 3C 264 | 1998-05-12 | 447.7 |
| 3C 270 | 1998-04-23 | 767.8 |
| 3C 272.1 | 1998-07-13 | 767.8 |
| 3C 274 | 1997-11-20 | 127.9 |
| 3C 293 | 1998-08-19 | 2751.8 |
| 3C 305 | 1998-07-19 | 2783.8 |
| 3C 317 | 1998-08-26 | 639.8 |
| 3C 338 | 1997-12-18 | 4159.8 |
| 3C 405 | 1997-12-16 | 1343.9 |
| NGC 6251 | 1998-07-06 | 543.5 |

Note. — Log of observations for the objects not included in the HST 1.6 $\mu$m near infrared snapshot program 10173 (PI: Sparks) (Madrid et al. 2006; Floyd et al. 2008). All data are taken with the same configuration with Camera NIC2 and F160W filter.

ies are know not to conform to case B we have used the observed near infrared broad line region ratios observed in type 1 AGN by Riffel et al. (2006) and Landt et al. (2008) to estimate the contamination in the F160W filter. This analysis shows the contamination to be $\lesssim 15\%$ for Broad Line Objects and $\lesssim 4\%$ for Narrow Line Objects and in both cases that is small enough not to affect our conclusions regarding the origin of the nuclear NIR emission.

Due to technical difficulties, 3C 410 and 3C 442 were only observed for 575.9 s, while all the remaining galaxies were observed for a total exposure time of 1151.8 s. A detailed description of the observations and data reduction can be found in Madrid et al. (2006).

Each galaxy was classified in two ways. Firstly, into FR I and FR II based on radio morphology (Fanaroff & Riley 1974): the radio morphological classification, mostly being adopted from Zirbel & Baum (1995). Secondly, based on the optical broad line strengths and narrow emission lines ratios (from Buttiglione et al. 2009, 2010) we classified them into the stand groupings of High and Low Ionization Galaxies (HIG and LIG) and Broad Line Objects (BLO). Note that the BLO objects belong to HIG class because they show high-ionization narrow emission lines. We adopt the HIG/LIG nomenclature to better represent the physical condition of the narrow line region gas in these objects. This classification is however entirely consistent with the HEG/LEG scheme widely adopted in the literature (e.g., Hine & Longair 1979; Laing et al. 1994; Buttiglione et al. 2010). Following Buttiglione et al. (2010) we introduced a 4th class of Extremely-Low Excitation Galaxies (ELEG), characterized by an extremely low value of [O III]/H$\beta \sim 0.5$, $\sim$6 times lower than usually observed in 3CR/LIG. In this work we consider ELEGs as a separate class of objects. The objects for which we do not have new spectral data are classified according to Jackson & Rawlings (1997). In the sample there is also one galaxy, 3C 198, characterized by a star forming spectrum (marked as "SF" in Table 2) and a BL Lac object (3C 371) which are not considered in the following statistical evaluations because of their unique properties among the objects of our sample. For one galaxy (3C 410) we could not find any reliable spectral classification in the literature.

## 3. RADIAL BRIGHTNESS PROFILE FITTING AND NUCLEAR LUMINOSITY MEASURING

The aim of this paper is to measure the NIR nuclear sources. In order to disentangle such a component from the underlying stellar emission of the host galaxy, it is necessary to model the distribution of the galactic light. To this purpose we derived the surface brightness profile of all our sources. Radial profiles can be derived using a number of different methods: ellipse fitting to the isophotes of the galaxies (e.g., Heraudeau & Simien 1996) obtaining a one-dimensional analysis (e.g., Baggett et al. 1998), and full two-dimensional analysis (e.g., Byun & Freeman 1995; Peng et al. 2002). In this paper, we adopted the first approach.

The "ellipse" task in IRAF STSDAS (Jedrzejewski 1987) is suitable to analyzing the axisymmetric structure, evident in most objects. This task allows us to trace the radial profile and radial changes in ellipticity, position angle, and coordinates of the center of the isophotes.

Most of the host galaxies of 3CR sources appear as smooth ellipticals in infrared. Only in few cases are distortions due to dust lanes, jets, or plumes. Before deriving the galaxy profile, we mask out all spurious objects such as stars, jets, dust lanes, bright, galaxy companions and residual diffraction patterns associated with bright stars. When dust features are present in the nuclear region we adopted a multi-stage strategy. To stabilize the fit in the radial range affected by the dust we started by fixing some or all fit-parameters to the values of the last isophote that is not affected by the dust. We then produce an initial model image and we subtracted it from the original data to unveil the presence of further faint sources and/or dust features, that were then also masked out and so on until no further feature were found.

In Fig. 1 we show the stages of the procedure to derive and to fit the radial brightness profile.

### 3.1. *Profile fitting*

The surface brightness profile can be fitted using a variety of functions. We used two different models, Sérsic and core-Sérsic. The former (Sersic 1968) is a law of the form:

$$I(r) = I_e \; e^{-b_n[(\frac{r}{r_e})^{\beta}-1]}$$

where $\beta$ is the concentration parameter and $\beta = 1/\mathrm{n}$, the inverse of the Sérsic index n. $\mathrm{I}_e$ is the intensity at the effective radius $\mathrm{r}_e$. For a Sérsic model with $0.5 \lesssim \mathrm{n} \lesssim 10$, $\mathrm{b}_n \approx 1.9992\mathrm{n} - 0.3271$ (e.g., Capaccioli 1989; Caon et al. 1994; Graham & Driver 2005).

The latter is composed of an outer Sérsic model and a inner power-law profile, suitable to describe the innermost part of the profile when the object shows a deficit toward the center with respect to the Sérsic law. Trujillo et al. (2004) argued that it is convenient to restrict the core-Sérsic model to an infinitely sharp transition between the Sérsic and power-law profiles at the break radius $\mathrm{r}_b$, assuming this form:

$$I(r) = I(b)\left[\left(\frac{r_b}{r}\right)^{\gamma}\theta(r_b - r) + e^{b_n\left(\left(\frac{r_b}{r_e}\right)^{\frac{1}{n}} - \left(\frac{r}{r_e}\right)^{\frac{1}{n}}\right)^{\frac{1}{n}}}\theta(r - r_b)\right]$$

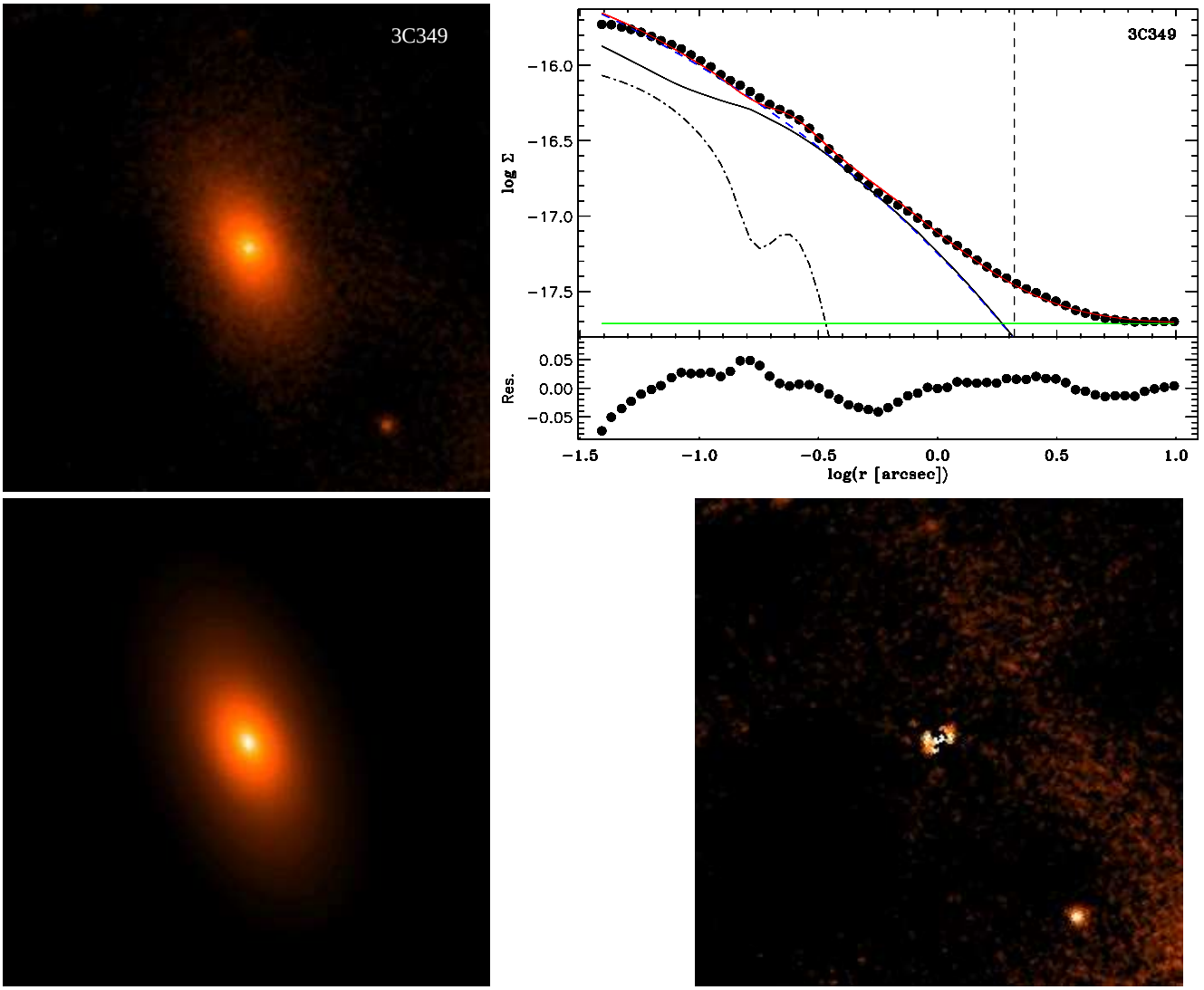


FIG. 1.— This figure summarizes the fitting procedure of the surface brightness profile (in this example 3C 349). In the upper left panel we show the original NICMOS image. The lower right panel presents the model image using the parameters obtained by the task ellipse. The lower left panel shows the residuals image (typically ∼10% in the nuclear region). The object in the S-W corner in the residual image was masked and not fitted by the ellipse task. All the images are ∼7″ wide. The upper right panel shows the fitting of the radial unidimensional brightness profile (in units of erg $s^{-1}$ $cm^{-2}$ $Å^{-1}$ $arcsec^{-2}$) with a Sérsic law (blue dashed curve), a nuclear component (black dot-dashed line) and a background level (green horizontal line). We take into account in the fit the convolution (black solid line) of the model with the instrumental PSF. The final model is the sum of each component and is the red solid line. The vertical dashed line gives the location of the effective radius $r_e$. In the lower region of the panel we show the residuals.

where $r_b$ separates the inner power law of logarithmic slope $\gamma$ from the outer part of the profile described by a Sérsic model. $\theta(r_b\text{-}r)$ is the Heaviside step function.

We fit the brightness profiles with both models by minimizing the residuals, leaving free to vary the 5 (or 7) variables: the background level, the three parameters describing the Sérsic (or five for core-Sérsic) model and the nuclear component. Fig. 2 illustrates four examples of fits to the NIR brightness profiles. In Sect. 3.2 we describe the method used to select the appropriate law for each galaxy.

To take into account the PSF effects, we convolved the models prior to the comparison with the data Capetti & Balmaverde (2005). The PSF of NICMOS-NIC2 at the center of the chip was derived using the TINYTIM program written by J. Krist. The PSF image was then convolved with a model galaxy with a power law profile, which represents the innermost region of a Sérsic/core-Sérsic model. This was done for a set of galaxy models with different profile slopes $\gamma'$, all of them having zero ellipticity. We then derived the radial profile of the convolved model galaxies using circular isophotes, and we calculated the intensity ratio between the convolved model galaxy and the original model galaxy for different radii. With this method we obtained a set of radial ratios for different values of the innermost slope that can be applied to the models to "simulate" the two-dimensional convolution.

The appropriate value of $\gamma'$ was measured as part of the fitting procedure. In the case of a Sérsic model, $\gamma'$ is the value of the logarithmic slope of the profile at 0.″1, which approximately corresponds to the resolution of NICMOS-NIC2. In the core-Sérsic model, $\gamma'$ is the logarithmic slope of the inner power-law profile.

Donzelli et al. (2007) already performed the fitting of the radial brightness profiles of 3CR sample with Sérsic

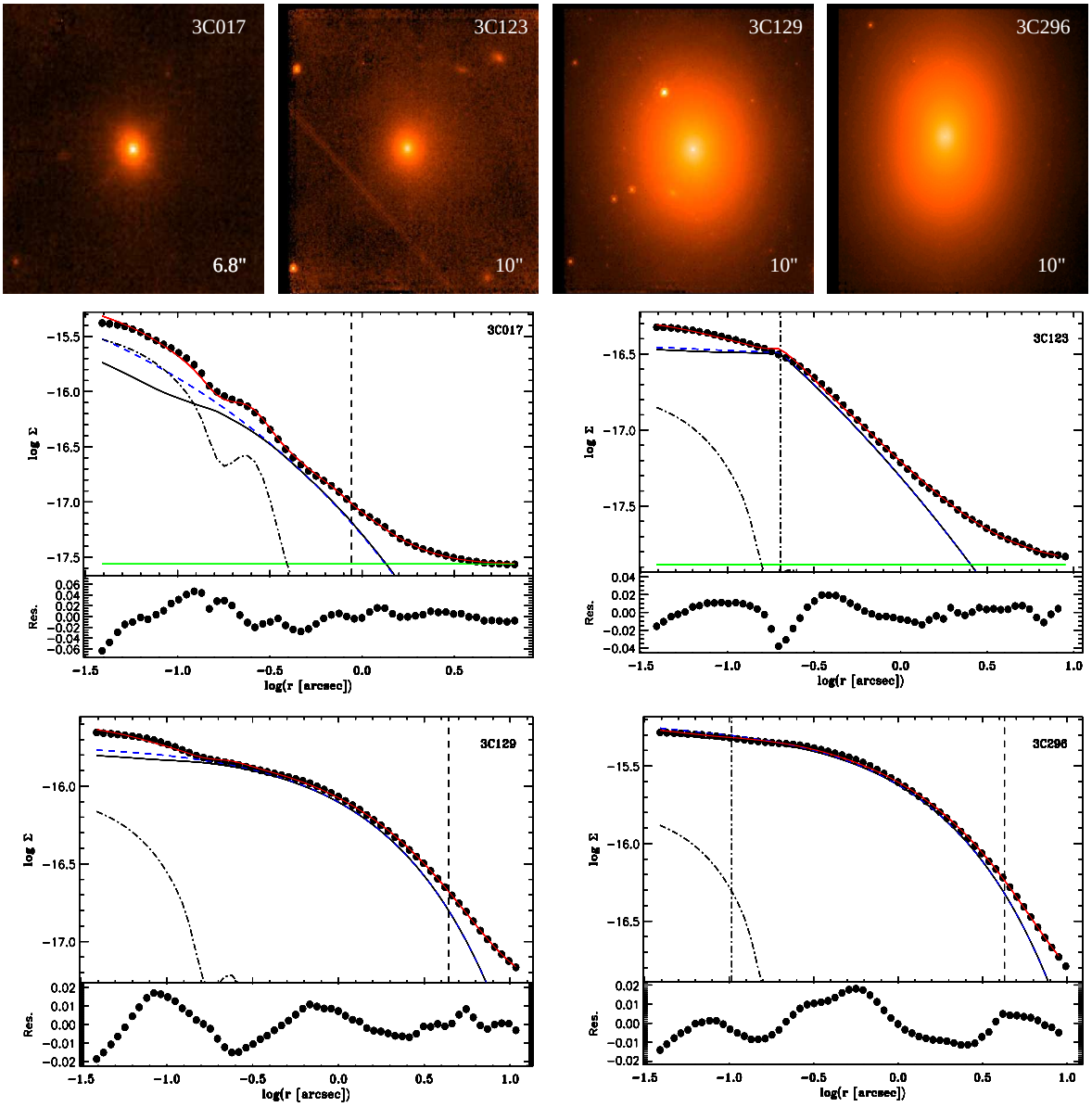


FIG. 2.— This figure shows four explicative fitting methods used. In the upper parts we report the NICMOS images of the 4 radio-galaxies. In the lower part each panel represents the modeling of the surface brightness profile with a Sérsic or a core-Sérsic. The description of lines are as in Fig. 1. We mark the position of the effective radius with a black vertical dot-dashed line and, for a core-Sérsic model, the break radius with a dashed vertical line. More in details we report four examples: in the upper left panel 3C 17 was fitted with a Sérsic model; in the upper right panel 3C 123 with a core-Sérsic model to obtain an upper-limit to its nuclear luminosity; in the lower left panel 3C 129 with a Sérsic model in the case of an weak nuclear source; and in the lower right panel 3C 296 with a core-Sérsic with a weak nuclear point source. In this last panel the nuclear source plotted in black dashed line is amplified of a factor 10 for a better visualization. In the plots of 3C 129 and 3C 296 the green horizontal line of the background level is absent because it is below the range of intensity shown.

law, focusing on their large scale behavior, thus not including the central region of the galaxies. For the objects in which Donzelli et al. (2007) found a disk-like component in the galaxy profile, we exclude from the fit the regions dominated by the disk. The parameter values found are mostly consistent with those of Donzelli et al. (2007) for the objects in which the nuclear component is not dominant with respect to the galaxy stellar emission. The resulting models produce residuals in the form of large scale fluctuations with a typical amplitude of $<$ 5%, indicative of the goodness of the fit.

Besides the parameters describing the host galaxy profile, the fitting procedure also yields the flux of the nuclear source.

To assess the reliability of the detection of a nuclear source we adopt the following operative approach. We extract the radial brightness profile using the IRAF "radprof" task and measure the nuclear FWHM, setting the background level at the intensity measured just beyond the nuclear point source at a radius of $\sim$0.3″. If the FWHM is consistent with that of the PSF ($\sim$ 0.14 arcsec), we took this as an indication of the presence of an unresolved source. Alternatively, if there was no evidence for a nuclear point source, we proceed to fit the profile with a core-Sérsic model leaving all parameters free to vary, but fixing $\gamma = 0$. This corresponds to the most conservative choice for $\gamma$ as it minimizes the galaxy contribution and maximizes the nuclear source. We con-

sider the nuclear flux thus derived as the upper limit to the intensity of the central source.

### 3.2. *Sérsic or core-Sérsic?*

The choice between Sérsic and core-Sérsic model for a given galaxy is related to the corresponding minimized $\chi^2$ value obtained after the fitting procedure. Since the core-Sérsic model includes more free parameters, the best core-Sérsic model usually will reproduce better the galaxy profile than the Sérsic model. Therefore, to determine the goodness of the fit, we use the "reduced" $\chi^2$ ($\chi^2_r$) $= \chi^2/(n-p)$, where $n$ is the number of fitted data points and $p$ is the number of fitted parameters, which can be either 3 or 5 for Sérsic or core-Sérsic models, respectively). We consider the best model that corresponds to the $\chi^2_r$ closest to the unity. Qualitatively, the choice can be justified by the form of the residuals. In fact, when fitting a core-Sérsic galaxy with a pure Sérsic model, the residuals in the central region show the characteristic S-shape, already discussed by Trujillo et al. (2004).

Nevertheless, since our objects are at distances of up to z = 0.3, we can misclassify a genuine core galaxy as a pure Sérsic due to an insufficient physical resolution of the image. The typical core size of an elliptical galaxy is ∼200 pc (e.g. Capetti & Balmaverde 2005; Faber et al. 1997; Ferrarese et al. 2006) which corresponds to 0.″14 at z = 0.15. Considering the objects at z > 0.15 with detected nuclei (excluding the BLOs, for which the nucleus outshines the host galaxy emission in the central region), for which there is ambiguity on the presence of a core, the typical discrepancy between the estimates of the nuclear luminosity obtained adopting either a Sérsic law or a core-Sérsic model is ∼ 30 %, and at most a factor of 2. The sources potentially involved in this ambiguity are only ∼15% of the sample and thus they do not alter the main results of this paper.

The presence of a bright point source may also limit our ability to see a possible shallow core and to discriminate between Sérsic and core-Sérsic models. However, in those cases (e.g. in the case of the BLOs, Fig.3), the difference between the nuclear fluxes obtained adopting the two different models is irrelevant, being smaller than ∼ 2%, thus well below the typical photometric error.

## 4. RESULTS

### 4.1. *Detection of nuclei*

In Table 2 we report the 1.6 $\mu$m NIR nuclear fluxes and luminosities for the sample measured with the procedure explained in Sect. 3. We also give the optical (R band), radio (nuclear at 5 GHz and large scale at 178 MHz) fluxes, and [O III] emission line luminosities for all the objects of the sample.

Here we examine the detection rate of the NIR central sources (Table 3), considering each radio-morphological and optical-spectral class separately. Overall, we detect nuclei in 64%±5% of the entire 3CR sample. We detect nuclei in 81%±8% and 58%±6% of the FR Is and FR IIs, respectively. Among the FR IIs, all of the BLOs have an unresolved nuclear point source, while the detection rate of nuclei in LIGs and HIGs is 44%±10% and 54%±9%, respectively. The only one BL Lac included in the sample has a bright nuclear source. The nucleus of 3C 410, the only spectroscopically unclassified FR II, is detected, while neither the ELEGs nor the star forming galaxy 3C 198 have an NIR nucleus. The different detection rates in the FR Is and FR IIs are not a consequence of the redshift distribution of the 3CR catalog. All FR II sources (HIG, LIG, and BLO) in our sample share a similar median redshift, and only the FR Is have a lower median $z$, because of their lower total power.

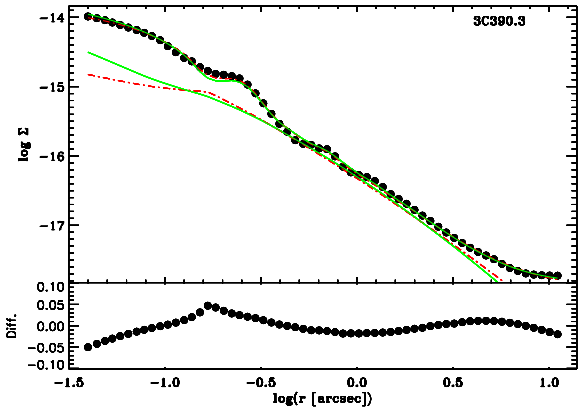


FIG. 3.— The surface brightness profile of 3C 390.3 fitted with a Sérsic model (green solid trace) and a core-Sérsic model (red dot-dashed trace). The lines below represent the two models used, which include the PSF-convolved galaxy model, the nuclear source and the background (the green solid and the red dot-dashed lines correspond to the Sérsic and core-Sérsic, respectively). In the lower panel we show the difference between the Sérsic-law and core-Sérsic models.

Due to the presence of upper limits, we use the Kaplan-Meier product-limit estimator (Kaplan & Meier 1958), which provides the mean value for a distribution with censored data, where the censoring is random, to measure the average value of NIR nuclear luminosities of each class (reported in Table 3). The BLOs have, on average, the brightest near infrared nuclear sources in the sample in luminosity ($<L_{IR}>$ = 1.6×10$^{29}$ erg s$^{-1}$ Hz$^{-1}$). The FR I nuclei are on average the faintest ($<L_{IR}>$ = 4.0×10$^{26}$ erg s$^{-1}$ Hz$^{-1}$). FR II LIGs and HIGs share a similar range of NIR luminosity and appear to bridge the gap between BLOs and FR Is. Undetected NIR nuclei are present for $F_{IR} < 10^{-27}$ erg cm$^{-2}$ s$^{-1}$ Hz$^{-1}$ and $L_{IR} < 2.5\times10^{28}$ erg s$^{-1}$ Hz$^{-1}$. However about one half of the detected nuclei have fluxes and luminosities below these values.

### 4.2. *Nuclei in the optical-infrared planes*

It is instructive to compare the NIR properties with those of the optical nuclei. In Fig. 4, left panel, we plot $F_o$-$F_{IR}$ and $L_o$-$L_{IR}$ for all objects in the sample. Not surprisingly, because of the relative proximity of the two bands, most of the points occupy a narrow strip parallel to the bisectrix of the planes. However, we have to be cautious in taking this plot at face value as it is sensitive to the presence of nuclear absorption and also to nuclear variability, since infrared and optical data were not obtained simultaneously.

The FR I galaxies (empty yellow circles) cover the whole range in optical and NIR fluxes (∼5 dex). The FR II LIGs (filled blue circles) are clustered in small optical and NIR flux range (∼2 dex) in the lower-left slide of the plane. The HIGs (filled green squares ) are also clustered, but with a slight tail towards higher flux, covering a wider range in both bands (∼3 dex) with respect

TABLE 2
Basic data for all 3CR source considered

| Name | z | FR - E.L. | Ref | log $F_{178MHz}$ | log $F_r$ | Ref | log $F_o$ | log $F_{IR}$ | log $L_{IR}$ | log $L_{[O\ III]}$ | Ref | Profile |
|---|---|---|---|---|---|---|---|---|---|---|---|---|
| 3C 15 | 0.073 | LIG | B09 | -21.80 | -23.42 | Z95 | <-28.05 | -27.42 | 27.55 | 40.46 | B09 | S |
| 3C 17 | 0.2197 | BLO | B09 | -21.70 | -23.08 | Z95 | -26.91 | -26.84 | 29.00 | 41.68 | B09 | S |
| 3C 20 | 0.174 | HIG | J97 | -21.37 | -25.48 | F97 | - | <-27.72 | <27.94 | 41.47 | L96 | cS |
| 3C 28 | 0.1953 | ELEG | B09 | -21.79 | <-26.70 | G88 | <-29.28 | <-29.64 | <26.10 | 40.67 | B09 | cS |
| 3C 29 | 0.0488 | FR I | B09 | -21.82 | -24.04 | M93 | -28.02 | -27.56 | 27.03 | 40.06 | B09 | S |
| 3C 31 | 0.017 | FR I | B09 | -21.77 | -24.04 | G88 | -27.61 | -27.44 | 26.29 | 39.41 | B09 | cS |
| 3C 33 | 0.059 | HIG | B09 | -21.28 | -24.52 | Z95 | - | <-27.14 | <27.64 | 42.05 | B09 | cS |
| 3C 33.1 | 0.1809 | BLO | B09 | -21.89 | -24.66 | Z95 | -27.5 | -27.12 | 28.57 | 42.03 | B09 | S |
| 3C 35 | 0.067 | LIG | B09 | -21.98 | -24.62 | Z95 | <-28.41 | <-28.30 | <26.59 | 39.87 | B09 | cS |
| 3C 52 | 0.28540 | LIG | B09 | -21.87 | -25.11 | C08 | - | <-28.85 | <27.18 | <40.84 | B09 | cS |
| 3C 61.1 | 0.184 | HIG | B09 | -21.51 | -25.43 | Z95 | - | <-28.57 | <27.13 | 42.20 | B09 | cS |
| 3C 66B | 0.0215 | FR I | B09 | -21.61 | -23.74 | G88 | -27.09 | -27.04 | 26.91 | 39.97 | B09 | cS |
| 3C 75N | 0.02215 | FR I | B09 | -21.59 | -24.29 | Z95 | - | <-28.48 | <25.48 | <39.80 | B09 | cS |
| 3C 76.1 | 0.03249 | FR I | B09 | -21.88 | -24.61 | G88 | - | <-28.29 | <25.99 | <39.75 | B09 | cS |
| 3C 79 | 0.256 | HIG | B09 | -21.52 | -24.76 | Z95 | -27.62 | -27.44 | 28.51 | 42.51 | B09 | S |
| 3C 83.1 | 0.0251 | FR I | B09 | -21.58 | -24.67 | R75 | -28.64 | -27.65 | 26.43 | <39.33 | B09 | cS |
| 3C 84 | 0.01756 | FR I | B09 | -21.39 | -21.37 | T96 | -25.61 | -25.47 | 28.28 | 41.53 | B09 | S |
| 3C 88 | 0.03022 | LIG | B09 | -21.82 | -23.72 | Z95 | -27.62 | -27.46 | 26.76 | 40.05 | B09 | S |
| 3C 98 | 0.03 | HIG | B09 | -21.45 | -24.97 | Z95 | <-28.55 | <-27.64 | <26.58 | 40.90 | B09 | cS |
| 3C 105 | 0.089 | HIG | B09 | -21.75 | -24.76 | Z95 | - | -27.82 | 27.3 | 41.29 | B09 | S |
| 3C 111 | 0.0485 | BLO | B09 | -21.19 | -22.93 | Z95 | -26.48 | -25.30 | 29.33 | 42.33 | B09 | S |
| 3C 123 | 0.2177 | LIG | B09 | -20.72 | -24.01 | H98b | <-29.39 | <-28.16 | <27.67 | 41.69 | B09 | cS |
| 3C 129 | 0.0208 | FR I | B09 | -21.33 | -24.99 | V82 | - | -27.48 | 26.43 | <39.75 | B09 | S |
| 3C 129.1 | 0.02220 | FR I | B09 | -21.98 | -25.51 | C08 | - | <-28.52 | <25.44 | <40.39 | B09 | cS |
| 3C 130 | 0.032 | FR I | H98a | -21.81 | -23.48 | H99 | - | <-28.04 | <26.24 | <40.59 | B09 | cS |
| 3C 132 | 0.214 | LIG | J97 | -21.91 | <-24.42 | Z95 | <-28.99 | <-28.03 | <27.78 | - | - | cS |
| 3C 133 | 0.2775 | HIG | B09 | -21.65 | -23.69 | N98 | -28.01 | -26.82 | 29.18 | 42.39 | B09 | S |
| 3C 135 | 0.1253 | HIG | B09 | -21.76 | -25.22 | Z95 | -28.04 | -27.60 | 27.80 | 41.85 | B09 | S |
| 3C 153 | 0.277 | LIG | B09 | -21.78 | <-26.28 | H98b | <-29.35 | <-27.94 | <28.07 | 41.26 | B09 | cS |
| 3C 165 | 0.2957 | LIG | B09 | -21.87 | -24.97 | H98b | -28.77 | -28.39 | 27.67 | 41.28 | B09 | S |
| 3C 166 | 0.245 | LIG | B09 | -21.83 | -23.19 | Z95 | -27.91 | -27.28 | 28.63 | 41.32 | B09 | S |
| 3C 171 | 0.2384 | HIG | B09 | -21.71 | -25.54 | Z95 | -29.40 | <-28.05 | <27.84 | 42.55 | B09 | cS |
| 3C 173.1 | 0.2921 | LIG | B09 | -21.81 | -24.86 | Z95 | - | -28.18 | 27.86 | 40.47 | B09 | cS |
| 3C 180 | 0.2200 | HIG | B09 | -21.82 | - | - | - | <-28.50 | <27.34 | 42.03 | B09 | cS |
| 3C 184.1 | 0.1182 | BLO | B09 | -21.89 | -25.10 | Z95 | -27.18 | -26.60 | 28.76 | 42.02 | B09 | S |
| 3C 192 | 0.0598 | HIG | B09 | -21.64 | -25.07 | Z95 | <-27.81 | <-27.92 | <26.88 | 41.22 | B09 | cS |
| 3C 196.1 | 0.198 | LIG | B09 | -21.73 | -24.11 | B89 | - | <-28.57 | <27.18 | 41.23 | B09 | cS |
| 3C 197.1 | 0.1301 | BLO | B09 | -22.09 | -25.13 | Z95 | -27.33 | -27.32 | 28.11 | 40.73 | B09 | S |
| 3C 198 | 0.0815 | SFG | B09 | -22.01 | <-25.77 | F78 | -27.02 | -26.96 | 28.09 | 40.82 | B09 | S |
| 3C 213.1 | 0.1937 | LIG | B09 | -22.18 | -23.22 | A95 | - | -27.52 | 28.22 | 40.78 | B09 | S |
| 3C 219 | 0.1744 | BLO | B09 | -21.39 | -24.12 | Z95 | -27.02 | -26.95 | 28.71 | 41.51 | B09 | S |
| 3C 223 | 0.1368 | HIG | B09 | -21.83 | -24.90 | Z95 | <-28.20 | -27.56 | 27.91 | 41.95 | B09 | S |
| 3C 223.1 | 0.107 | HIG | B09 | -22.22 | -25.03 | H98b | <-28.09 | -26.65 | 28.62 | 41.39 | B09 | S |
| 3C 227 | 0.0861 | BLO | B09 | -21.52 | -24.62 | Z95 | -26.26 | -25.70 | 29.40 | 41.60 | B09 | cS |
| 3C 234 | 0.185 | HIG | B09 | -21.58 | -23.83 | Z95 | -26.61 | -26.04 | 29.66 | 42.84 | B09 | S |
| 3C 236 | 0.1005 | LIG | B09 | -21.84 | -23.71 | Z95 | <-28.18 | -27.50 | 27.72 | 40.72 | B09 | S |
| 3C 258 | 0.1650 | LIG | B09 | -22.01 | - | - | - | <-28.38 | <27.24 | 39.94 | B09 | cS |
| 3C 264 | 0.0206 | FR I | B09 | -21.58 | -23.70 | G88 | -26.62 | -26.64 | 27.28 | 39.07 | B09 | cS |
| 3C 270 | 0.0074 | FR I | B09 | -21.26 | -23.51 | G88 | -27.97 | -27.05 | 25.96 | 37.89 | B09 | cS |
| 3C 272.1 | 0.0037 | FR I | B09 | -21.71 | -23.75 | G88 | -26.88 | -27.07 | 25.35 | 38.13 | B09 | cS |
| 3C 274 | 0.0037 | FR I | B09 | -19.98 | -22.40 | G88 | -26.06 | -25.52 | 26.90 | 38.80 | B09 | cS |
| 3C 277.3 | 0.0857 | HIG | B09 | -22.05 | -24.91 | G88 | -28.61 | <-27.08 | <28.09 | 40.78 | B09 | cS |
| 3C 284 | 0.239 | HIG | B09 | -22.21 | -25.65 | Z95 | - | <-28.53 | <27.37 | 41.26 | B09 | cS |
| 3C 285 | 0.0794 | HIG | B09 | -21.95 | -25.10 | Z95 | -29.38 | -27.93 | 27.11 | 40.40 | B09 | S |
| 3C 287.1 | 0.2159 | BLO | B09 | -22.09 | -23.29 | Z95 | -27.11 | -26.41 | 29.42 | 41.43 | B09 | S |
| 3C 288 | 0.246 | FR I | Z95 | -21.72 | -24.53 | G88 | -28.94 | -28.71 | 27.40 | - | - | cS |
| 3C 293 | 0.0452 | LIG | B09 | -21.90 | -24.81 | G88 | - | -28.09 | 26.47 | 39.70 | B09 | cS |
| 3C 296 | 0.0237 | FR I | B09 | -21.89 | -24.10 | G88 | -28.25 | -28.13 | 25.92 | 39.65 | B09 | cS |
| 3C 300 | 0.27 | HIG | B09 | -21.75 | -24.92 | Z95 | -28.20 | -27.83 | 28.16 | 41.64 | B09 | S |
| 3C 303 | 0.141 | BLO | B09 | -21.95 | -23.69 | Z95 | -26.83 | -26.49 | 29.01 | 41.51 | B09 | S |
| 3C 305 | 0.04164 | HIG | B09 | -21.80 | -24.50 | G88 | - | <-28.10 | <26.40 | 40.93 | B09 | cS |
| 3C 310 | 0.054 | FR I | B09 | -21.26 | -24.10 | G88 | -28.24 | <-27.07 | <27.69 | 39.95 | B09 | cS |
| 3C 314.1 | 0.1197 | ELEG | B09 | -21.98 | <-26.00 | G88 | <-28.81 | <-27.37 | <28.09 | 39.49 | B09 | cS |
| 3C 315 | 0.1083 | FR I | B09 | -21.75 | -23.75 | G88 | - | -27.76 | 27.52 | 40.69 | B09 | cS |
| 3C 317 | 0.0342 | FR I | B09 | -21.33 | -23.41 | M93 | -27.67 | -27.05 | 27.31 | 40.25 | B09 | cS |
| 3C 319 | 0.192 | LIG | B09 | -21.82 | <-25.80 | Z95 | <-28.33 | <-27.77 | <27.96 | <39.91 | B09 | cS |
| 3C 321 | 0.096 | HIG | B09 | -21.87 | -24.41 | Z95 | - | -27.64 | 27.55 | 40.73 | B09 | cS |
| 3C 323.1 | 0.264 | BLO | B09 | -22.00 | -24.28 | Z95 | -25.83 | -25.77 | 30.20 | 42.45 | B09 | S |
| 3C 326 | 0.089 | LIG | B09 | -22.11 | -24.78 | Z95 | <-28.04 | -27.87 | 27.25 | 40.23 | B09 | cS |
| 3C 332 | 0.1515 | BLO | B09 | -22.02 | -24.90 | Z95 | -26.76 | -26.08 | 29.47 | 41.57 | B09 | S |
| 3C 338 | 0.03035 | FR I | B09 | -21.33 | -23.99 | G88 | -27.78 | -28.17 | 26.08 | 39.44 | B09 | cS |

TABLE 2
CONTINUED

| Name | z | FR - E.L. | Ref | log $F_{178MHz}$ | log $F_r$ | Ref | log $F_o$ | log $F_{IR}$ | log $L_{IR}$ | log $L_{[O\ III]}$ | Ref | Profile |
|---|---|---|---|---|---|---|---|---|---|---|---|---|
| 3C 346 | 0.162 | FR I | S91 | -21.96 | -23.66 | G88 | -27.42 | -27.01 | 28.73 | 41.59 | G94 | S |
| 3C 348 | 0.154 | ELEG | B09 | -20.45 | -25.00 | M93 | -28.88 | <-27.34 | <28.34 | 40.17 | B09 | cS |
| 3C 349 | 0.205 | HIG | J97 | -21.88 | -24.60 | H98b | -27.62 | -27.39 | 28.39 | 41.82 | R89 | S |
| 3C 353 | 0.03043 | LIG | B09 | -20.63 | -23.69 | Z95 | <-28.70 | <-27.99 | <26.24 | 40.05 | B09 | cS |
| 3C 357 | 0.167 | LIG | B09 | -22.09 | -25.15 | Z95 | <-28.73 | <-27.94 | <27.68 | 40.70 | B09 | cS |
| 3C 371 | 0.051 | BLLac-LIG | B09 | -22.43 | -23.04 | P81 | -25.56 | -24.91 | 29.75 | 40.84 | B09 | S |
| 3C 379.1 | 0.256 | HIG | B09 | -22.13 | -25.26 | S85 | <-28.74 | <-28.05 | <27.89 | 41.51 | B09 | cS |
| 3C 381 | 0.1605 | HIG | B09 | -21.78 | -25.11 | Z95 | <-28.08 | -27.24 | 28.36 | 42.12 | B09 | S |
| 3C 382 | 0.0578 | BLO | B09 | -21.70 | -23.64 | Z95 | -25.05 | -24.91 | 29.86 | 41.65 | B09 | S |
| 3C 388 | 0.091 | LIG | B09 | -21.61 | -24.10 | Z95 | -27.88 | -27.83 | 27.31 | 40.54 | B09 | S |
| 3C 390.3 | 0.0561 | BLO | B09 | -21.32 | -23.36 | Z95 | -25.70 | -25.42 | 29.32 | 41.96 | B09 | S |
| 3C 401 | 0.201 | LIG | B09 | -21.68 | -24.27 | Z95 | -28.15 | -28.26 | 27.51 | 40.76 | B09 | S |
| 3C 402 | 0.0239 | LIG | B09 | -22.00 | -24.29 | Z95 | -27.43 | <-27.87 | <26.15 | <39.34 | B09 | cS |
| 3C 403 | 0.059 | HIG | B09 | -21.75 | -24.92 | Z95 | -28.14 | -26.97 | 27.81 | 41.62 | B09 | S |
| 3C 403.1 | 0.05540 | LIG | J97 | -21.87 | - | - | - | <-27.97 | <26.76 | - | - | cS |
| 3C 405 | 0.05607 | HIG | O75 | -19.06 | -23.46 | Z95 | - | -27.84 | 26.90 | 41.96 | O75 | cS |
| 3C 410 | 0.248500 | FR II | D96 | -21.46 | -22.83 | C08 | - | -26.25 | 29.68 | - | - | S |
| 3C 424 | 0.126988 | FR I | B09 | -21.85 | -24.67 | B92 | <-28.61 | -27.77 | 27.64 | 40.60 | B09 | S |
| 3C 430 | 0.0556 | LIG | B09 | -21.47 | -24.77 | S84 | - | <-27.60 | <27.14 | 40.23 | B09 | cS |
| 3C 433 | 0.1016 | HIG | B09 | -21.25 | -25.24 | G88 | - | -26.51 | 28.73 | 41.50 | B09 | S |
| 3C 436 | 0.2145 | HIG | B09 | -21.75 | -24.61 | Z95 | - | <-28.06 | <27.76 | 41.25 | B09 | cS |
| 3C 438 | 0.29 | LIG | B09 | -21.35 | -24.60 | Z95 | <-29.18 | <-28.28 | <27.76 | <41.08 | B09 | cS |
| 3C 442 | 0.0263 | FR I | B09 | -21.79 | -25.68 | G88 | -28.82 | -27.75 | 26.35 | 39.14 | B09 | cS |
| 3C 445 | 0.057 | BLO | B09 | -21.61 | -23.42 | Z95 | -25.49 | -25.31 | 29.45 | 42.39 | B09 | S |
| 3C 449 | 0.01708 | FR I | B09 | -21.94 | -24.44 | G88 | -27.53 | -27.22 | 26.58 | 39.13 | B09 | S |
| 3C 452 | 0.0811 | HIG | B09 | -21.26 | -23.81 | Z95 | -28.16 | <-27.89 | <27.16 | 41.19 | B09 | cS |
| 3C 459 | 0.2199 | BLO | B09 | -21.59 | -22.82 | Z95 | - | -26.65 | 29.18 | 41.73 | B09 | S |
| 3C 465 | 0.0301 | FR I | B09 | -21.42 | -23.57 | G88 | -27.50 | -27.39 | 26.86 | 39.71 | B09 | cS |
| NGC 6251 | 0.02471 | FR I | P84 | -22.00 | -23.05 | J86 | -26.82 | -26.28 | 27.80 | 39.70 | S81 | cS |

Description of the table: Col.(1): name; Col.(2): redshift; Col.(3): Fanaroff & Riley and optical spectral classifications. For simplicity, we mark as FR I all radio galaxies with FR I-like radio morphology and LIG-like optical spectrum, as LIG all radio galaxies with FR II-like radio morphology and LIG-like optical spectrum, as HIG (BLO) all radio galaxies with FR II-like radio morphology and HIG-like optical spectrum with the absence (presence) of broad emission lines. References (Col. 4): B09 Buttiglione et al. (2010), J97 Jackson & Rawlings (1997), H98a Hardcastle (1998), Z95 from Zirbel & Baum (1995), S91 Spencer et al. (1991), O75 Osterbrock & Miller (1975), D96 de Koff et al. (1996), P84 Perley et al. (1984); Col.(5): flux density at 178 MHz in erg $s^{-1}$ $cm^{-2}$ $Hz^{-1}$ (in these logarithmic units -23 corresponds to 1 Jy); Col.(6): nuclear radio flux density at 5 GHz in erg $s^{-1}$ $cm^{-2}$ $Hz^{-1}$. References (Col. 7): B92 Black et al. (1992) (8.3 GHz), G88: Giovannini et al. (1988), L91: Leahy & Perley (1991), M93: Morganti et al. (1993), R75 Riley & Pooley (1975), T96 Taylor et al. (1996), Z95 Zirbel & Baum (1995), N98 Nilsson (1998), H98b Hardcastle et al. (1998) (8.4 GHz) F97: Fernini et al. (1997), V82: van Breugel & Jagers (1982), H99: Hardcastle (1999), B89: Baum & Heckman (1989), F78: Fomalont & Bridle (1978), A95: Akujor & Garrington (1995), P81: Pearson & Readhead (1981), S85: Spangler & Sakurai (1985) (1.5GHz), S84: Spangler et al. (1984), J86: Jones et al. (1986), C08: A. Capetti, priv. com.. Radio core data at frequencies different from 5 GHz were converted to 5 GHz using a flat ($\alpha = 0$) spectral index; Col.(8): nuclear optical flux density in erg $s^{-1}$ $cm^{-2}$ $Hz^{-1}$ (Chiaberge et al. 1999, Chiaberge et al. 2000a and Chiaberge et al. 2002a) in R band; Col.(9): nuclear 1.6 $\mu$m near infrared flux density in erg $s^{-1}$ $cm^{-2}$ $Hz^{-1}$; Col.(10): nuclear 1.6 $\mu$m near infrared luminosity in erg $s^{-1}$ $Hz^{-1}$; Col.(11): [O III]$\lambda\lambda$5007 luminosity in erg $s^{-1}$. References (Col.12): B09 Buttiglione et al. (2009), O75 Osterbrock & Miller (1975), S81 Shuder & Osterbrock (1981), L96 Lawrence et al. (1996), R89 Rawlings et al. (1989). Col.(13): type of model used to fit the NIR surface brightness profile.

TABLE 3
Detections of nuclei in the sample

| Class | Nuclei | Upper lim. | Tot. | % | Log $L_{IR}$ |
|---|---|---|---|---|---|
| FR I | 21 | 5 | 26 | 81 | 26.7 ± 0.2 |
| FR II | 42 | 31 | 73 | 58 | – |
| LIG | 11 | 14 | 25 | 44 | 26.9 ± 0.2 |
| HIG | 15 | 13 | 28 | 54 | 27.5 ± 0.2 |
| BLO | 15 | 0 | 15 | 100 | 29.2 ± 0.1 |
| ELEG | 0 | 3 | 3 | 0 | – |
| SFG | 0 | 1 | 1 | 0 | – |
| UNDEF | 1 | 0 | 1 | 100 | – |
| BLLac | 1 | 0 | 1 | 100 | – |
| Tot. | 64 | 36 | 100 | 64 | |

Note. — Detection rate of 1.6 $\mu$m near infrared nuclei for each class. The ELEG (Extremely Low Ionization Galaxies) are 3C 28, 3C 314.1, and 3C 348. The BL Lac is 3C 371, the Star forming Galaxy (SFG) is 3C 198 and the Undefined object (UNDEF) is 3C 410 because of the lack of spectral data. LIGs, HIGs, BLOs, ELEGs, SFG and UNDEF belong to FR II class. Column description: (1) class; (2) number of detected nuclei; (3) number of undetected nuclei; (4) total number of objects for each class; (5) percentage of detection; (6) the mean value and their errors of the NIR luminosities for each class with the Kaplan-Meier statistics.

to FR II LIGs. The BLOs (filled red triangles) show the highest optical and NIR fluxes of the sample.

In the $L_O$-$L_{IR}$ plane (Fig. 4, middle panel) we find that FRIs exhibit the lowest luminosities. FR II LIGs and HIGs are present at increasing optical and NIR luminosities. Finally, the BLOs are by far the most powerful objects.

To highlight the presence of outliers in the $L_O$-$L_{IR}$ plane, in Fig. 4 (right panel) we show the ratio between NIR and optical nuclear luminosities plotted vs. the NIR nuclear luminosity. Most objects lie within ∼0.5 dex of the dashed line representing $\nu L_{IR}/\nu L_o = 1$. Note that most of the nuclei that are found above this line (i.e. showing an NIR excess with respect to the optical emission) belong to the HIG class. We discuss the origin of this behavior of the HIGs in more detail in Sect. 5.4.

### 4.3. *Nuclei in the radio-infrared planes*

In order to investigate the origin of the NIR nuclei, we now explore possible correlations between the properties of the infrared nuclear emission and those of the radio cores. Fig. 5, left panel, shows the IR nuclear flux $F_{IR}$ plotted vs. the radio core flux $F_r$. The FR Is (empty yellow circles) cover the whole range of flux spanned by the sample, both in the radio and in the NIR. HIGs (filled green squares) and FR II LIGs (filled blue circles) are clustered in the central region of the plane. The BLOs (filled red triangles) are located in the top-right quadrant, at higher radio and NIR fluxes. A similar distribution of the points is evident in the plane defined by the radio and the NIR core luminosities (Fig. 5, right panel). However in the $L_r$-$L_{IR}$ plane the distributions are stretched because of the common dependence of the two quantities on distance. The FR I galaxies have radio core luminosities that are on average lower than those of FR IIs. This is expected because the Fanaroff-Riley morphological radio classification in FR I and FR II corresponds to different total luminosities at 178 MHz, and a positive trend links total and core radio luminosity (Giovannini et al. 1988).

A clear trend is visible for FR Is both in the $F_r$-$F_{IR}$ and $L_r$-$L_{IR}$ planes (Fig. 5). FR II LIGs nuclei also show a trend in both planes, even if they cover a smaller range in radio core flux (2 dex for the NIR detected nuclei) with respect to FR Is. Conversely, there is no evident link between radio and NIR emission for HIGs and BLOs.

In order to assess the presence of correlations, we performed a statistical analysis using the Astronomy Survival Analysis (ASURV) package (Lavalley et al. 1992). This package is available under IRAF/STSDAS and provides us a tool to deal with censored data (Feigelson & Nelson 1985, Isobe et al. 1986). Note that the method we use is based on the assumption that the censored data are uniformly distributed. In order to determine whether this approach is viable, we apply the censoring analysis only when the above assumption is satisfied. We initially check the location of the non-detected data points with respect to the entire range of available data.

We used the "schmittbin" task (Schmitt 1985) to calculate the associated linear regression coefficients for two set of variables. Operatively, we carried out this procedure twice, obtaining two linear regressions: firstly considering the former quantity as the independent variable and the latter as the dependent one, secondly switching the roles of the variables. The best fit is represented by the bisector of these two regression lines. This followed the suggestion of Isobe et al. (1990) that consider such a method preferable for problems that require a symmetrical treatment of the two variables. In order to estimate the quality of the linear regression, for small data sets (N < 30) we also derived the generalized Kendall's $\tau$ (Kendall 1983) between the two variables, using the "bhkmethod" task. Otherwise, we used Spearman's rank order correlation coefficient, using the "spearman" task (Akritas 1989) only for large data sets (N > 30, for the cases of HIGs and the whole sample). The statistical parameters of all the linear regressions are reported in Table 4.

The trend shown by FR Is (Fig. 5, empty yellow circle points) in the $F_r$-$F_{IR}$ plane corresponds to a linear correlation coefficient[8] of r = 0.79. The probability to obtain this level of correlation from two independent variables is $P = 2.2\times10^{-5}$. The statistical parameters are even better in the radio-infrared luminosity plane, where the linear correlation coefficient is r = 0.85, with an associated probability $P = 8.9\times10^{-7}$. The dispersions of these correlations are ∼0.51 and ∼0.48 dex, for fluxes and luminosities, respectively. The generalized Kendall's $\tau$ coefficient, which allows us to include censored data, is higher for the luminosities ($\tau = 1.18$) than that for the fluxes ($\tau = 1.00$). The associated probabilities of no correlation, are 0.0002 and <0.0001, respectively. Note that the slopes of both linear regressions are consistent with unity.

We now turn our attention to the possible presence of correlations for FR II galaxies. FR II LIGs show a linear correlation in both planes of Fig. 5. Considering only the detected nuclei, the linear correlation coefficient is

[8] This is derived using the VLA measurements for the radio cores. If we consider the radio cores fluxes from VLBI, we obtain a similar correlation, statistically indistinguishable from that obtained using the VLA cores. This is because the core fluxes measured with VLA and VLBI differ only marginally (see the Appendix).

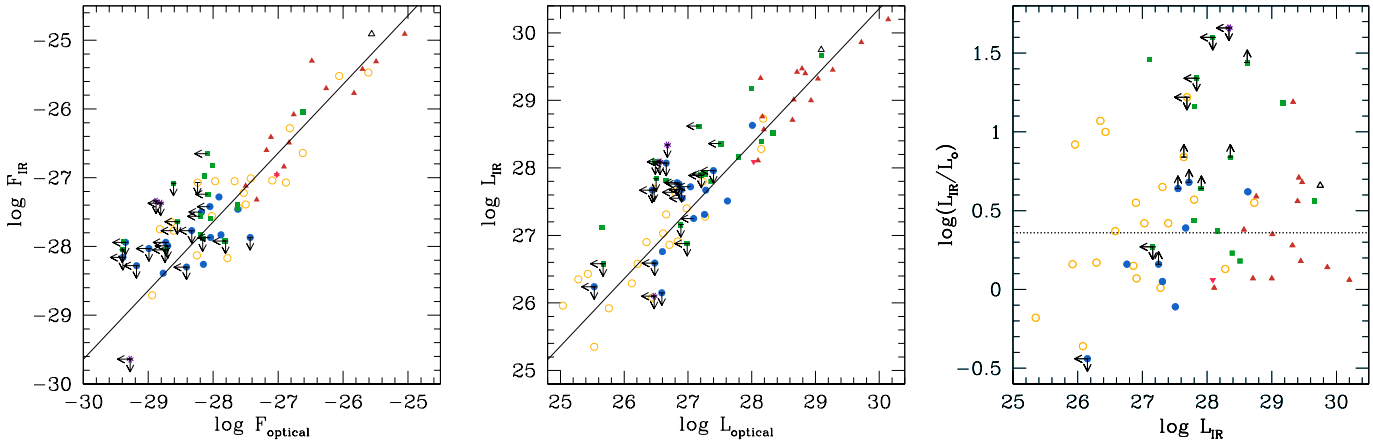


FIG. 4.— In left panel, log$F_o$-log$F_{IR}$ (in units of erg s$^{-1}$ cm$^{-2}$ Hz$^{-1}$); in median panel, log$L_o$-log$L_{IR}$; in right panel, log$L_{IR}/L_o$-log$L_{IR}$ (in units of erg s$^{-1}$ Hz$^{-1}$). In these plots the empty yellow circles represent the FR Is, the filled blue circles the FR II LIGs, the filled green squares the HIGs and the filled red triangles the BLOs, the purple asterisks the ELEGs, the empty black triangle the BL Lac (3C 371), and the filled pink reversed triangle the SFG (3C 198). The solid or dashed lines present in these plots are the line representing the unity of the ratio $\nu L_{IR}/\nu L_o$. In the right-panel plot, although the same factor $L_{IR}$ appears in both axes, its aim is not to find a relation or a trend, but to better point out the outliers in $\log(L_{IR}/L_o)$.

r = 0.89 in the $F_r$-$F_{IR}$ plane, with a probability of a no correlation of P = $1.0\times10^{-4}$. The censoring statistics gives a generalized Kendall's coefficient $\tau$ = 0.77 with a probability, P = 0.0012, that a fortuitous correlation appears at a level measured by our test statistic. In $L_r$-$L_{IR}$ plane for FR II LIGs a linear relation (dotted line in Fig. 5, right panel) is also statistically supported: the linear correlation coefficient is r = 0.93 (P = $1.1\times10^{-5}$). The radio-infrared core luminosity relation for FR II LIGs has a slope of 0.9±0.3.

Therefore, an important result of our analysis is that the correlations found for FR Is and FR II LIGs nuclei are consistent with each other within the errors. This result is shown in Fig. 6 where for more clarity we have marked these two classes with different symbols.

For HIGs and BLOs the absence of a trend is confirmed by the results of the statistical analysis and in particular by the high probabilities that their distribution in the $L_r$-$L_{IR}$ plane is random (see the statistical parameters in Tab. 4).

### 4.4. *Spectral indices*

In order to derive the multi-wavelength properties of the nuclei, it is useful to analyze the broad-band radio-infrared spectral index $\alpha_{r-IR}$. In Fig. 7 we show the empirical distribution in $\alpha_{r-IR}$ for the four different classes (FR I, FR II LIG, HIG and BLO). Note that the average value of the radio-IR spectral index distributions shifts towards lower values from FR II LIGs to the BLOs, with FRIs and HIGs having intermediate values. This indicates that with respect to the IR flux, the FR II LIGs are the most radio-powerful objects. Another intriguing aspect worth noting is that even though FR II LIGs and FR Is behave similarly in the radio-IR plane, as they define the same correlations, their distribution of $\alpha_{r-IR}$ are slightly different. In fact, FR II LIGs have on average a slightly higher $\alpha_{r-IR}$ than the FR I galaxies. On the other hand, HIGs and BLOs show an near infrared excess with respect to the radio emission and therefore their $\alpha_{r-IR}$ spectral indices are on average lower than for the other two classes.

To assess the presence of any significant differences between the spectral index distribution of the different classes, we can make use of the 'twosampt' task, available in the ASURV package. The task computes several nonparametric two-sample tests, giving a variety of ways to test whether two censored samples are drawn from the same parent population.

We utilize the Peto-Prentice statistic (Peto & Peto 1972), which is a generalization of standard test for uncensored data, such as the Wilcoxon (Wilcoxon 1945) and Kolmogorov-Smirnov (Chakravarti & Roy 1967) test. This statistical test quantifies a distance between the empirical distribution functions of two samples. The null distribution of this statistic is calculated under the null hypothesis that the samples are drawn from the same distribution.

We statistically measure the different distributions of spectral indices between FR Is and FR II LIGs and between HIGs and BLOs. We can assert that FR Is and FR II LIGs are not drawn from the same parent population at the 97% confidence level. The same holds for the HIG and BLO classes at the 99% confidence level.

### 4.5. *Comparison with FR Is' radio-optical correlation*

Chiaberge et al. (1999) measured the optical nuclear fluxes for most FR I radio galaxies in the 3CR catalog. The optical detection rate is similar to that found for the FR Is of our sample. For the sub-sample of objects for which the total radio luminosity at 178 MHz is lower than the FR I/FR II break (corresponding to $L_{178\,MHz}$ $\sim 2\times10^{33}$ erg s$^{-1}$ Hz$^{-1}$), they found a tight linear correlation between the optical and radio nuclear fluxes with a dispersion of ∼0.4 dex. In order to compare the radio-infrared and radio-optical correlations we selected the 15 FR Is in common with the sample of Chiaberge et al. (1999) (namely 3C 29, 3C 31, 3C 66B, 3C 83.1, 3C 84, 3C 264, 3C 270, 3C 272.1, 3C 274, 3C 296, 3C 317, 3C 338, 3C 442, 3C 449, and 3C 465)[9]. We estimate the linear regression between radio and near infrared fluxes

[9] Although 3C 277.3 satisfies the selection criteria, we excluded the object from this sample since from an careful inspection of its radio maps we revised its radio-morphological classification from FR I to FR II.

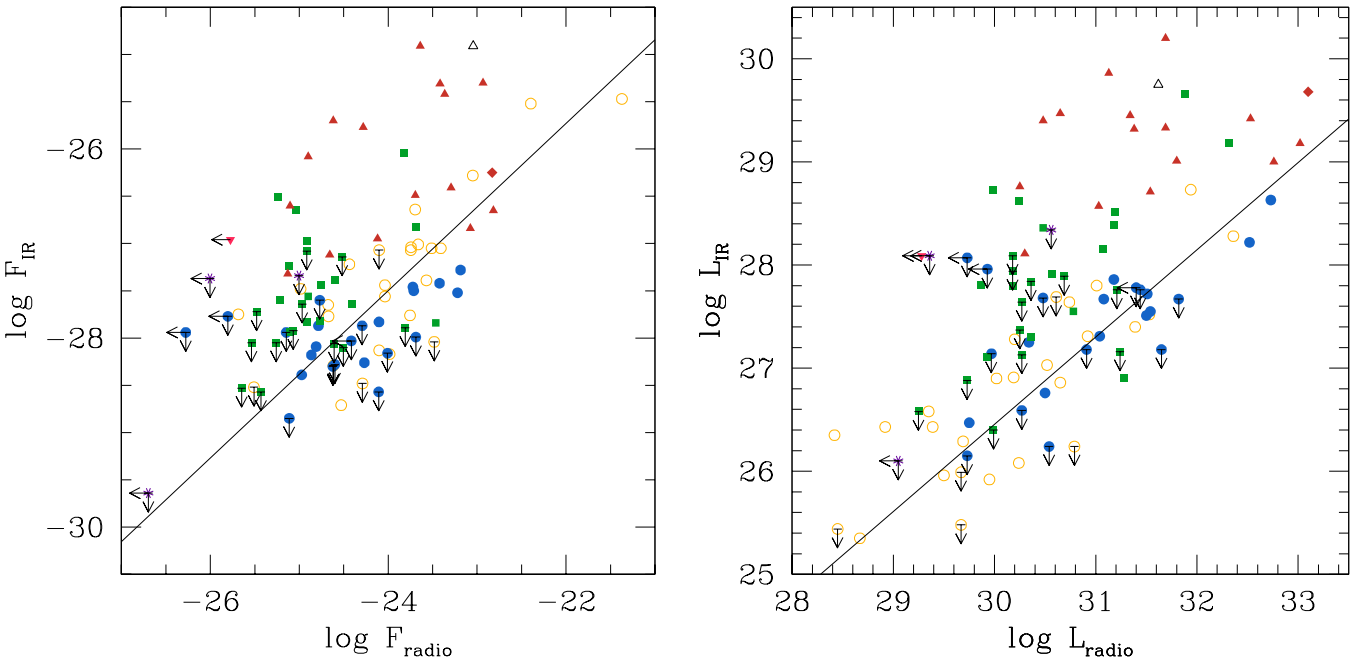


FIG. 5.— Left panel: radio core flux vs. near infrared nuclear flux (in units of erg s$^{-1}$ cm$^{-2}$ Hz$^{-1}$). Right panel: radio core luminosity vs. near infrared nuclear luminosity (in units of erg s$^{-1}$ Hz$^{-1}$). In these plots the empty yellow circles represent the FR Is, the filled blue circles the FR II LIGs, the filled green squares the HIGs and the filled red triangles the BLOs, the purple asterisks the ELEGs, the empty black triangle the BL Lac (3C 371), the filled pink reversed triangle the SFG (3C 198), and the filled red diamond is the undefined object (3C 410). The solid line represents the linear correlation found for FR Is and FR II LIGs.

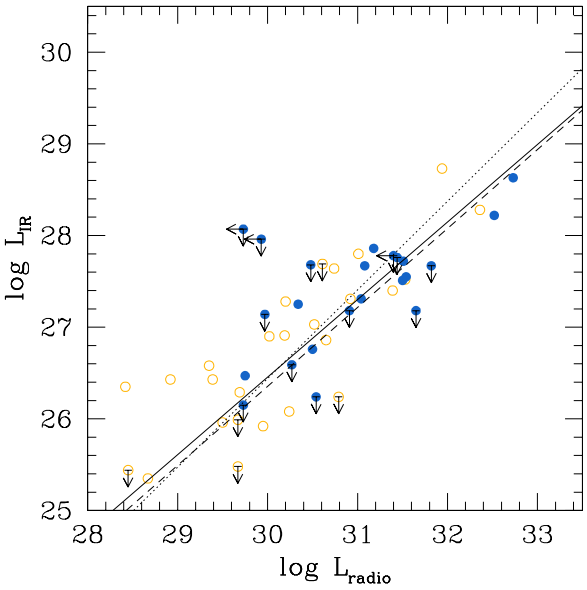


FIG. 6.— Radio core luminosity vs. near infrared nuclear luminosity (in units of erg s$^{-1}$ Hz$^{-1}$) for FR Is (empty yellow points) and FR II LIGs (blue points). We show the linear correlations: the solid line is obtained for FR Is and FR II LIGs, the dotted line for FR Is only, and the dashed line for FR II LIGs only.

for this sub-sample: the correlation coefficient is r = 0.82 (P = 2.2×10$^{-4}$) and the dispersion is ∼0.49 dex. We tested that the dispersions of the two relations, $F_r$-$F_{IR}$ and $F_r$-$F_o$, are not statistically different at a significance level of 95%.

## 5. DISCUSSION

In the following we consider the properties of each group of 3CR radio galaxies separately.

### 5.1. *FR I galaxies*

The presence of a linear correlation between FR I radio and NIR cores, both in flux and luminosity, argues for a real physical connection between the two variables. This is indeed not the result of a common dependence on redshift of the two quantities, as shown by the fact that the statistical parameters of both correlations are similar. Following Chiaberge et al. (1999), that interpreted the optical-radio core correlation as the indication that synchrotron emission dominates the nuclear emission at both wavelengths, we argue that the correlations between the radio and the NIR nuclei described here can be explained by the same physical mechanism. More precisely, the presence of such a tight correlation between the NIR and radio cores indicates that non thermal (synchrotron) radiation dominates their emission at all considered wavelengths, including the X-ray as shown by Balmaverde et al. (2006). Capetti et al. (2007) found that the optical HST nuclei of 9 3CR/FR I, which also belongs to our sample, are highly polarized. This strengthens the synchrotron origin of their nuclear emission.

The correlations among NIR, VLA and VLBI cores and the fact that the fluxes of the VLA and VLBI cores (see Appendix) are essentially equal suggest that the NIR cores are typically produced on scales consistent with or even smaller than the size of the VLBI cores. In fact, according to various jet models (e.g., Ghisellini et al. 1985), it is likely that the radio and the IR/Optical radiation is produced in the innermost region of the jet, close to the black hole ($\lesssim 10^{16}$ cm), while the radio is emitted on larger scales.

The dominance of synchrotron radiation even in the NIR indirectly confirms that accretion in most FR I nuclei occurs at low rates and/or with low radiative ef-

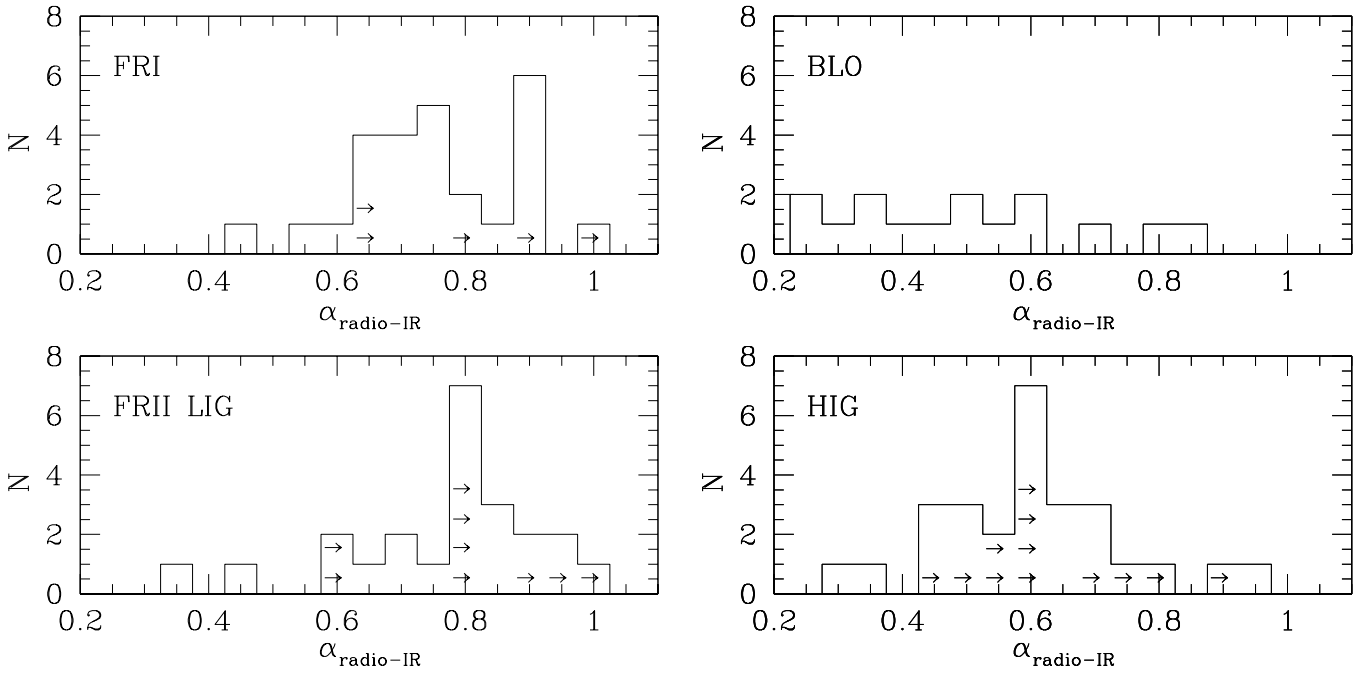


FIG. 7.— Histograms of radio-infrared spectral indices $\alpha_{r-IR}$ for each sub-class of the sample. The arrows represent the lower limits data.

TABLE 4
SUMMARY OF THE STATISTICAL ANALYSIS OF THE LINEAR REGRESSIONS.

| Relation | Class | $N_d$ | $N_c$ | $r_d$ | $P_{r_d}$ | $\rho_d$ or $\tau_d$ | $P_{\rho_d}$ or $P_{\tau_d}$ | $\rho$ or $\tau$ | $P_\rho$ or $P_\tau$ | $rms_x$ | $rms_y$ | m | q |
|---|---|---|---|---|---|---|---|---|---|---|---|---|---|
| $F_r$-$F_{IR}$ | FR I | 21 | 5 | 0.788 | $2.2\times10^{-5}$ | 1.181 | 0.0002 | 0.997 | 0.0002 | 0.477 | 0.543 | 1.0±0.2 | -3±5 |
| $F_r$-$F_{IR}$ | FR I [a] | 15 | 0 | 0.834 | 0.00011 | 1.238 | 0.0013 | / | / | 0.442 | 0.542 | 0.8±0.2 | -8±6 |
| $F_r$-$F_{IR}$ | FR I [b] | 15 | 1 | 0.855 | $4.9\times10^{-5}$ | 1.257 | 0.0011 | 1.233 | 0.0006 | 0.394 | 0.407 | 1.0±0.3 | -3±6 |
| $F_{vlbi}$-$F_{IR}$ | FR I | 15 | 1 | 0.866 | $3.0\times10^{-5}$ | 1.239 | 0.0012 | 1.217 | 0.0007 | 0.380 | 0.291 | 1.3±0.3 | 5±5 |
| $F_r$-$F_{IR}$ | LIG | 11 | 12 | 0.890 | 0.00010 | 1.490 | 0.0014 | 0.775 | 0.0012 | 0.168 | 0.298 | 0.6±0.3 | -14±15 |
| $F_r$-$F_{IR}$ | FR I+LIG | 32 | 17 | 0.781 | $4.1\times10^{-8}$ | 0.743 | <0.0001 | 0.645 | <0.0001 | 0.445 | 0.511 | 0.9±0.2 | -7±14 |
| $F_r$-$F_{IR}$ | HIG | 15 | 12 | 0.150 | 0.59 | -0.095 | 0.804 | 0.296 | 0.218 | 0.542 | 0.544 | 1.2±0.4 | 3±24 |
| $F_r$-$F_{IR}$ | BLO | 15 | 0 | 0.348 | 0.20 | 0.514 | 0.181 | / | / | 0.680 | 0.727 | 1.0±0.4 | -3±9 |
| $L_r$-$L_{IR}$ | FR I | 21 | 5 | 0.854 | $8.9\times10^{-7}$ | 1.324 | <0.0001 | 1.077 | <0.0001 | 0.420 | 0.532 | 1.0±0.2 | -3±6 |
| $L_r$-$L_{IR}$ | FR I [b] | 15 | 1 | 0.898 | $5.4\times10^{-6}$ | 1.276 | 0.0009 | 1.167 | 0.0008 | 0.392 | 0.417 | 1.0±0.2 | -3±5 |
| $L_{vlbi}$-$L_{IR}$ | FR I | 15 | 1 | 0.903 | $4.1\times10^{-6}$ | 1.333 | 0.0005 | 1.183 | 0.0007 | 0.384 | 0.347 | 1.1±0.2 | -7±5 |
| $L_r$-$L_{IR}$ | LIG | 11 | 12 | 0.931 | $1.1\times10^{-5}$ | 1.491 | 0.0014 | 0.696 | 0.0011 | 0.211 | 0.306 | 0.9±0.3 | 0±12 |
| $L_r$-$L_{IR}$ | FR I+LIG | 32 | 17 | 0.890 | $1.8\times10^{-8}$ | 0.900 | <0.0001 | 0.688 | <0.0001 | 0.363 | 0.487 | 0.8±0.2 | 1±18 |
| $L_r$-$L_{IR}$ | HIG | 15 | 12 | 0.503 | 0.056 | 0.514 | 0.181 | 0.461 | 0.054 | 0.637 | 0.606 | 1.3±0.5 | -13±27 |
| $L_r$-$L_{IR}$ | BLO | 15 | 0 | 0.2398 | 0.39 | 0.152 | 0.692 | / | / | 0.488 | 0.802 | 0.8±0.5 | 4±14 |

NOTE. — Column description: (1) relation studied; (2) class of radio-galaxies considered for the relation; (3) number of detected nuclei included in the relation considering both the quantities; (4) number of censored nuclei included in the relation considering both the quantities; (5) $r_d$ linear correlation coefficient for the relation obtained only with the detected data; (6) $P_{r_d}$ probability associated with $r_d$ that the correlation is not present; (7) $\rho_d$ Spearman's rank coefficient (if $N_d > 30$) or $\tau_d$, generalized Kendall's tau (if $N_d < 30$), for the relation obtained only with the detected data; (8) $P_{\rho_d}$ (or $P_{\tau_d}$) probability associated with $\rho_d$ (or $\tau_d$) that the correlation is not present; (9) $\rho$ Spearman's rank coefficient (if $N_{d+c} > 30$) or $\tau$, generalized Kendall's tau (if $N_{d+c} < 30$), considering all the data; (10) $P_\rho$ (or $P_\tau$) probability associated with $\rho$ (or $\tau$) that the correlation is not present; (11) $rms_x$, rms on x-axis for the relation obtained only with the detected data; (12) $rms_y$, rms on y-axis for the relation obtained only with the detected data; (13)-(14) slope coefficient m and intercept coefficient q for the linear regression (y = m*x + q) obtained considering all the data. In the rows marked with *a* the considered sample is composed of the FR I objects with $L_{178MHz} < 2\times10^{26}$ W Hz$^{-1}$ shared with sample studied by Chiaberge et al. (1999). In the rows marked with *b* the considered sample is composed of the FR Is whose the VLBI radio core measurement is available. With LIG we consider FR II LIG.

ficiency (e.g., Baum et al. 1995, Chiaberge et al. 1999, Allen et al. 2006, Balmaverde et al. 2008). However, there are exceptions to this result: the clearest example is possibly 3C 120 (a radio galaxy which is formally not part of 3CR sample) which displays a radio morphology typical of FR Is (e.g. Walker et al. 2001) while its nuclear emission shows the clear signature of broad lines and radiatively efficient accretion (Phillips & Osterbrock 1975). On the other hand, exceptions are also present among BL Lacs, the putative "beamed" counterpart of LIG population. A number of BL Lacs also show (faint) narrow and/or broad emission lines (e.g. Vermeulen et al. 1995) and others have FR II-like extended radio emission (e.g. Antonucci 1986; Kharb et al. 2010).

Chiaberge et al. (1999) pointed out that the dispersion of the radio-optical correlation ($\sim$ 0.4 dex) is consistent with dust absorption, provided that the $A_V$ is randomly distributed among the sources and does not exceed $\sim$ 2 mag. Since the extinction in H-band is 4.5 times lower than in the optical R-band, the observations presented in this work are far less sensitive to the presence of dust along the line of sight than those in Chiaberge et al. (1999). Therefore, one would expect the dispersion of the infrared-radio correlation to be smaller than that of the radio-optical, if that is due to absorption. Our results instead show that the rms of the two correlations are similar. Thus, the most likely explanation for the scatter is that variability of the nuclei plays a fundamental role, while the effect of absorption is less significant. Indeed, this is supported by the variability observed for the nuclear flux of 3C 317 (Chiaberge et al. 2002b) and of 3C 274 (Tsvetanov et al. 1998, Perlman et al. 2003). Conversely, the presence of dust appears to play a role in dimming the nuclear flux on the UV (Chiaberge et al. 2002b). Note that data in the literature indicate that the radio core variability is typically at 10% over a time scale of several years (Hine & Scheuer 1980; Ekers et al. 1983). Therefore the main source of the scatter in the radio-NIR correlation is mostly likely due to a variable NIR nuclear component.

Furthermore, the region of the jet base that produces the optical/NIR emission in FR Is is likely to be mildly relativistic (e.g., Chiaberge et al. 1999; Xu et al. 1999b). Therefore, we consider the effects of Doppler boosting on our results. Firstly, the range in NIR nuclear luminosity might be enhanced by relativistic beaming, which would boost (or de-boost) the emission of FR I nuclei, depending on the viewing angle. Objects seen under a small angle between the line-of-sight and the jet axis would appear boosted, while objects observed closer to the plane of the sky would be de-boosted. Secondly, nuclear variability might be enhanced by relativistic beaming when the flux variation is associated with 1) a change in the jet bulk Lorentz factor, or 2) a change in the jet direction, which would result in a different angle between the jet direction and the line-of-sight.

However, as noted by Chiaberge et al. (1999), the bulk Lorentz factor of the component responsible for the nuclear optical/NIR emission is most likely around $\Gamma \sim 2$ and the source is possibly a "slower" shear layer in the jet. Therefore, the effects of relativistic beaming should not dramatically affect our results.

Are the NIR data telling us something new about the presence of optically and geometrically thick obscuring tori in FR Is with respect to the optical observations? The results derived considering the UV, optical, and NIR bands are only apparently in contradiction. In fact, the median absorption toward FR I nuclei derived from UV observations is $A_V \sim 1.3$. This corresponds to only 0.2 mag in H band, negligible with respect to a dispersion of $\sim$0.5 dex, and to $\sim$ 3 mag at 2500 Å.

The detection rate of FR I nuclei in the NIR (81%) is similar to that found in the R band by Chiaberge et al. (1999). All sources with an optical nucleus also show a NIR counterpart, except 3C 310. Instead, in 3C 75N a faint dust lane prevents the study of its nuclear regions in the optical, while its NIR core is clearly detected. Furthermore, the absence of FR I outliers in the $L_{IR}/L_O$ ratio (see right panel of Fig. 4) can be interpreted as a hint that the *detected* FR I nuclei are not affected by significant absorption ($A_V \lesssim 2$ mag).

The reason for the non-detection of some of the FR I NIR nuclei might instead be due to a small contrast between the nucleus and the host galaxy stellar emission. Assuming that the radio and the near infrared emission of FR I nuclei are intrinsically tightly correlated, the intensity of their radio cores provides a robust prediction of their infrared nuclear flux. Following the analysis on the B2 radio-galaxies by Capetti et al. (2002), we plot the radio core fluxes of all FR Is against the galaxies central surface brightness (Fig. 8). Four out of the five undetected nuclei are indeed among those with the lowest predicted contrast against the galaxy emission. 3C 310 is the only object that does not have an NIR detected nucleus and apparently shows an rather larger contrast with galaxy emission than that of the other four non-detected nuclei. However, since its optical nucleus is detected, its NIR non-detection is likely not due to a obscuration.

Summarizing, we argue that in most cases we have a direct view of FR I nuclei and that the few undetected NIR central sources are below the detection threshold set by the contrast with the underlying host galaxy emission. Note that the detection of massive dusty structures in the central regions of some FR Is (e.g. Okuda et al. 2005, Das et al. 2005) does not contrast with our result that the NIR nuclei are mostly unobscured. In fact dust is distributed in large kpc-scale geometrically thin disks which do not appear to 'hide' the nuclei to our line-of-sight.

### 5.2. *FR II: Low Ionization Galaxies LIG*

Chiaberge et al. (2002a) found that the nuclei of FR II LIGs lie on the FRI radio-optical correlation. The sample of FR II LIGs available in this work is substantially larger than the sample those authors considered, both because of the increasing number of FR II LIG identifications and of the larger sample size. This allows us to establish the presence of a correlation between the radio and the NIR emission within the sample of FR II LIGs itself. An important result is that the correlations for FR Is and FR II LIGs are statistically indistinguishable. This strengthens the hypothesis that the LIGs are FR II galaxies with FR I-like nuclei. Such a nuclear similarity implies that non-thermal synchrotron radiation (e.g., from a relativistic jet) dominates their nuclear emission in NIR band and that accretion may occur with a radiatively inefficient process and/or at low accretion rates in

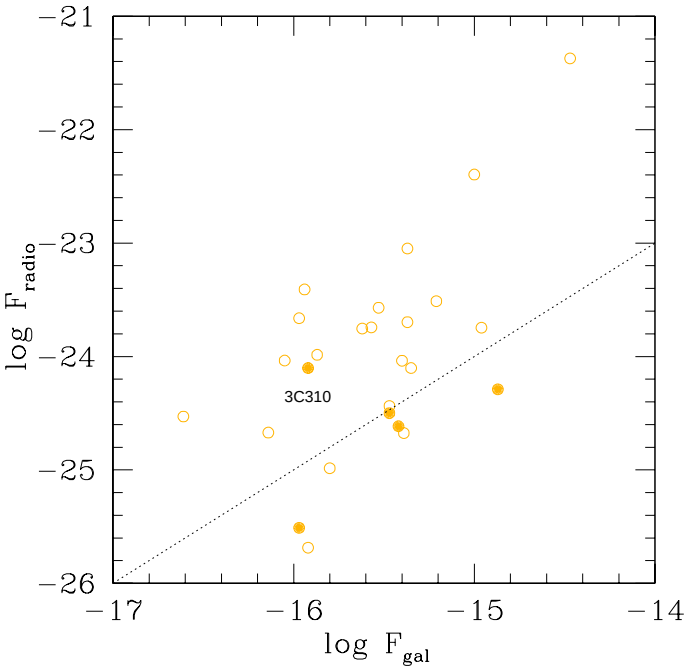


FIG. 8.— Radio core flux density, log $F_{radio}$ (erg $s^{-1}$ $cm^{-2}$ $Hz^{-1}$), versus central (on a circular region of r=0.″15) surface brightness of the host galaxy, log $F_{gal}$ (erg $s^{-1}$ $cm^{-2}$ $Å^{-1}$ $arcsec^{-2}$) for all FR I. Objects with detected near infrared nuclei are marked with empty yellow circles, while those with non-detection by filled yellow circles. The dotted line marks a constant ratio between the radio core and galaxy emission.

FR II LIGs as well.

The large fraction of FR II LIGs in our sample (∼33% of the FR IIs) proves that these objects are not rare exceptions in the FR II class. This class of objects show nuclear properties similar to those of FR Is, whereas their radio morphologies span the range from classical double to X-shaped, and from compact source to Fat Double (FD). The FD morphology (Owen & Laing 1989) consists of a FR II radio structure with elongated and diffuse lobes and sometimes with prominent jets, and may be considered as an intermediate class between FR Is and FR IIs. At least half of the FR II LIG sample show a FD radio morphology. The large variety of extended radio morphologies associated with a central LIG-like AGN makes it difficult to understand how the properties of the core and extended radio structures are related (e.g. Bicknell 1984, 1994; Gopal-Krishna & Wiita 2001). The existence of FR II LIGs as a class shows that radiatively inefficient accretion disks are able to produce jets that give rise to the typical large scale FR II morphology. Another possibility is that FR II LIGs constitute an evolutionary (or transient) state of the life of the FR II class. However, the environment of FR II LIGs is different from that of other classes of FR IIs, as FR II LIGs are predominantly found in dense groups or clusters (Chiaberge et al. 2000a; Hardcastle 2004). That seems to rule out the evolutionary scenario.

The lower detection rate of FR II LIG nuclei with respect to that of FR Is is most likely due to the reduced contrast between their faint IR nuclei and the surrounding stellar emission of the host galaxy, because of the higher redshift of FR II LIGs as compared to that of FR Is. In fact, the fraction of detected FR II LIG nuclei decreases as redshift increases, from 55 % for z<0.15 to 29 % for z>0.15. However, at this stage we cannot rule out that the presence of significant obscuration along the line of sight to the FR II LIGs with non-detected nuclei might also contribute to the reduce the fraction of detected FR II LIG nuclei. The best way to probe obscuration in FR II LIGs is through X-ray spectral analysis. FR II LIGs indeed seem to lack significant absorbing column densities, $N_{\rm H} \sim 10^{23}$ $cm^{-2}$ (Hardcastle et al. 2006).

The fact that the central engines of FR II LIGs and FR Is are similar (i.e., they are both unobscured and lack a significant broad line region) has important bearings for the unification schemes. As pointed out by Laing et al. (1994), the broad distribution in core-dominance is consistent with FR II LIGs being a randomly oriented sample. Since FR II LIGs also appear to lack significant broad emission lines, when observed along the jet axis, these objects would appear as BL Lacs, in agreement with Chiaberge et al. (2000b) in light of their findings in the optical band. Such a unification scenario, which was previously explored by Jackson & Wall (1999) based on the optical spectral properties of FR II LIGs, is in apparent contrast with zeroth order unification scheme which associates all FR II with quasars. However, besides being in agreement with our results, it may also account for the presence of BL Lacs with an FR II morphology.

Nevertheless, FR II LIGs do show some differences with respect to FR Is. In fact, as shown in Fig. 7, FR II LIGs and FR Is have slightly different radio-IR broadband spectral indices. If FR II LIGs are indeed the counterparts of BL Lacs with FR II radio morphology, the spectral index discrepancy can be explained in the framework of the so-called "blazar sequence" (Fossati et al. 1998). Such a scenario predicts a smooth transition in the properties of blazars' spectral energy distribution (SED). In blazars, the synchrotron emission peak is observed to shift towards lower frequencies as the radio luminosity at 5 GHz increases. The luminosity of the synchrotron emission peak also increases following the same trend. This gives rise to a sequence having high energy peaked BL Lacs at the lowest luminosities, low energy peaked BL Lacs at intermediate luminosities, and flat spectrum radio quasars at the highest bolometric powers. In Fig. 9 we schematically show what the effect of such a scenario on the broad band spectral indices would be. As the peak in the SED shifts towards lower frequencies, $\alpha_{r-IR}$ steepens. Therefore, the steeper spectral indices we found in FR II LIGs might be explained in terms of a slightly higher 5GHz core luminosity with respect to that of FR Is. FR II LIGs would thus correspond to intermediate power blazars such as the low-energy peaked BL Lacs.

The possibility that, conversely, the change in $\alpha_{r-IR}$ is due to the redshift of the SED for the more distant objects can be excluded using the formula presented by Trussoni et al. (2003). The formula, originally derived for estimating the effect of relativistic beaming, can be used to to account for the effect of redshift on the broadband spectral indices, by substituting $R_\delta$, the ratio of the beaming factors, with $(1 + z)$. The variation in the radio-infrared spectral due to the frequency shift for an object at z∼0 moved to z=0.3 is only $\Delta\alpha_{r-IR} \sim 0.02$, a correction that has a negligible effect on the results.

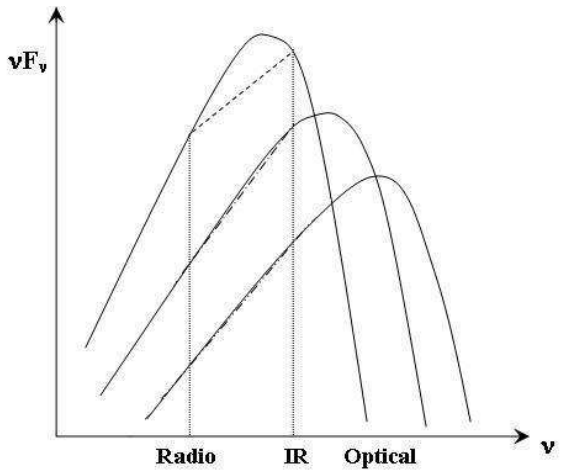


FIG. 9.— The Spectral energy distributions (SED) of three blazars in order to explain the so-called scenario (Fossati et al. 1998). In the three blazars, the synchrotron emission peak shifts towards lower frequencies as the radio luminosity at 5 GHz increases, which also corresponds to a higher luminosity of the synchrotron emission peak. The dashed lines represent the radio-infrared spectral indeces of each SED. As the peak in the SED shifts towards lower frequencies, $\alpha_{r-IR}$ steepens.

### 5.3. *FR II: Broad Line Objects BLO*

According to the standard unification scheme, the BLOs are objects where the nuclear region is unobscured along our line of sight (e.g. Barthel 1989; Antonucci & Ulvestad 1985). This idea is supported by the fact that all the NIR nuclei are detected for BLOs.

The BLOs show a strong NIR excess, of up to two orders of magnitude in luminosity, with respect to the correlation defined by the FR I (and FR II LIG) radio-infrared nuclei (Fig. 5, right panel). A similar excess was already found in the optical band by Chiaberge et al. (2002a) interpreted that as thermal emission from the accretion disk.

Let us now explore the origin of their NIR nuclear light. The infrared-optical spectral index for BLOs covers the range $\alpha_{IR-o} \sim 0$ - 2 (with the exception of 3C 111 for which $\alpha_{IR-o} = 3.3$). Such a large range might result from a wide distribution of spectral indices (see Fig. 11 in Elvis et al. 1994). In addition, variability may smear the intrinsic distribution. Therefore we consider the median value $\alpha_{IR-o} = 0.95$. This value indicates that the Spectral Energy Distribution (SED) of BLOs is essentially flat in a $\nu L_\nu$ representation.

To better investigate the origin of NIR emission in the BLOs of our sample we compare their properties with those of the radio-loud QSOs (RLQSO) from Elvis et al. (1994). As demonstrated by those authors, the averaged SED of QSOs shows a minimum at $\sim 1\mu$m. For wavelengths shorter than $1\mu$m the light is likely to be dominated by the accretion disk (i.e., the big blue bump), while for longer wavelengths a broad peak is observed, which is interpreted as emission from hot dust. The flat spectral index of BLOs is an indication that, on average, the optical and NIR HST observations are located on opposite sides of the SED minimum. Therefore, by analogy with RLQSOs, we then conclude that in most 3CR/BLOs the H band light is mainly produced by the high temperature tail of the hot dust emission, located at the inner face of the obscuring material.

We estimate a spectral index of $\alpha_{IR-o} = 0.35$ from the averaged SED of RLQSOs after adopting the mean redshift of BLOs (z = 0.14). The difference of the spectral indices between RLQSOs and BLOs can be accounted by an NIR/optical flux ratio of the BLOs larger by a factor $\sim$2 than that of RLQSOs. This is an indication of a relatively larger contribution from the dust in infrared emission of BLOs than that observed in RLQSOs. Furthermore, reminding the reader that the RLQSO have optical and NIR luminosities a factor of 100-1000 higher than those of the 3CR/BLOs, there is a dependence of the optical-infrared spectral index on the luminosity of the object.

### 5.4. *FR II: High Ionization Galaxies HIG*

At odds with the results found for FR II LIGs and FR Is, the NIR emission of HIG nuclei does not correlate with the radio cores. Furthermore, most of the detected nuclei exceeds the emission of FR Is and FR II LIGs at a given radio-core luminosity, suggesting an additional component dominating over the jet emission, similar to what we found for the BLOs.

However, HIG nuclei are substantially fainter than those of the BLOs, on average by a factor of 50. This is expected in a standard unification scheme, since the HIGs are considered to be the obscured counter parts of BLOs. This result indicates that substantial obscuration is still present in the NIR, despite the reduced effects of dust in the H band.

In order to investigate the origin of NIR emission in HIGs, we follow the method described by Marchesini et al. (2005) who studied a complete subsample of the 3CR radio catalog, which includes all HIGs with z < 0.3, observed in K′ band from the ground. They first estimated the ionizing luminosity, $L_{ion} = L_{NLR}$ $C^{-1}$ =0.0675 × $L_{[OIII]}$ (e.g. total luminosity in narrow lines, $L_{NLR}$, estimated from [O II] and [O III], Rawlings & Saunders 1991) for HIGs and BLOs assuming the same covering factor for the two classes, C = 0.01. Then, for each source, Marchesini et al. (2005) plotted $L_{ion}/L_{IR}$ against $L_o/L_{IR}$, which are both sensitive to nuclear obscuration. They found that HIGs do not follow the 'reddening line' (see caption of Fig. 10) in such a plane, as one might expect if they were simply "partially obscured" BLO nuclei. This lead them to conclude that a substantial role is played by scattered nuclear light.

With respect to Marchesini et al. (2005) our analysis can rely on *direct* measurements of the NIR nuclei and these are available for a larger number of HIG, due to better sensitivity of the HST images to faint IR nuclei. Furthermore, we also have NIR data for the nuclei of BLO, thus providing a more robust estimate of the location of unreddened sources.

In agreement with the results Marchesini et al. (2005) we found that only a few HIGs are located along the reddening line in Fig. 10 but this is clearly not the case for the whole population.

We then include the effects of scattered nuclear light. In this scenario a dusty torus attenuates the direct nuclear light by an extinction $A_{V,torus}$ and a fraction $f$ of the total nuclear light $L_{IR}$ is scattered into our line of sight (see Eq. 3 and in Marchesini et al. 2005). The effects of varying $A_{V,torus}$ is as follows: an increase of the nuclear obscuration simply corresponds to an increase of

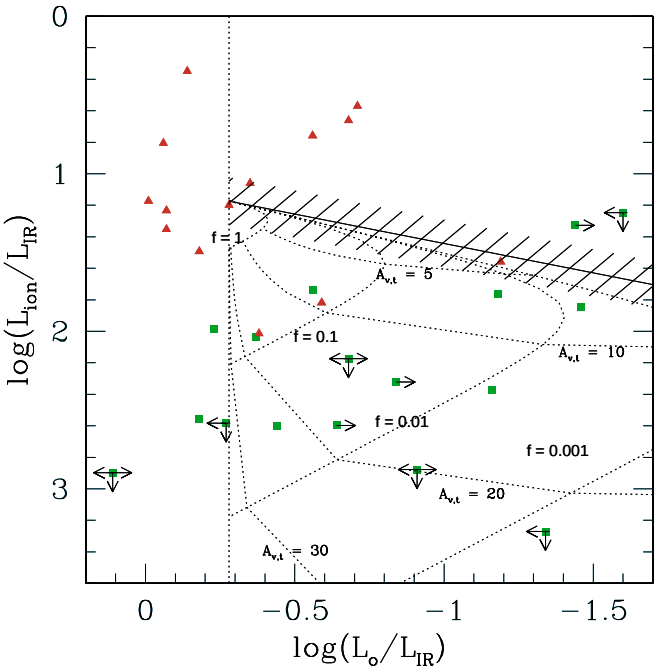


FIG. 10.— Ratio between the ionization luminosity $L_{ion}$ and $\nu L_{IR}$ versus the ratio between $L_o$ and $L_{IR}$. The BLOs are the red triangles and the HIGs the green squares. The solid oblique line is the 'reddening line' that purely obscured objects should follow. The origin of this line is determined by the ratios measured for BLOs, i.e. $\log(L_{ion}/\nu L_{IR}) = 1.17\pm0.15$ and $\log(L_O/L_{IR}) = -0.28\pm0.11$. The dashed region reproduces the uncertainty of its origin. The dotted vertical line corresponds to the average value of $\log(L_O/L_{IR})$ measured for BLOs. The grid of dotted curves represent the effects of varying the nuclear $A_{v,t}$ and the fraction of scattered light $f$ (see the Eq.3 in Marchesini et al. (2005)).

$L_{ion}/\nu L_{IR}$. The behavior of $L_o/L_{IR}$ is more complex: initially, an increase of the absorption moves the point (starting from the average location of BLO) to the right, along the reddening line. At larger values of $A_{V,torus}$ the direct (transmitted) optical light becomes fainter than the scattered component, while the infrared nucleus is still substantially unaltered. At even higher values of $A_{V,torus}$, the infrared transmitted component starts to decrease; since the scattered optical component remains constant this causes an increase of $L_O/L_{IR}$, producing a turnover in the source path. The track ends at the same ratio of $L_o/L_{IR}$ found for BLOs, but shifted downward by a factor linked to $A_{V,torus}$. The location of the turnover instead depends on the fraction of scattered light $f$, moving to smaller $L_o/L_{IR}$ and to larger $L_{ion}/\nu L_{IR}$ with decreasing $f$.

Because both the IR and the optical emission is most likely variable, therefore non-simultaneous measurements may lead to large errors in the estimate of the intrinsic $L_O/L_{IR}$. Nevertheless, this does not compromise the analysis: while a handful HIGs can be interpreted with being purely obscured BLOs, most of them (approximately 3/4 of the sample) require obscuration as well as scattered light, in the range of $10<A_{V,torus}<30$ and $0.02\%< f <10\%$ respectively. This agrees with the general results of Marchesini et al. (2005) (they derived a fraction of $\sim$70%) and also considering HIGs on a object-by-object basis.

Our analysis of the brightness profiles of the 3CR sources always assumed that the nuclear NIR components are unresolved. While for the other classes of 3CR galaxies the nuclear sources are directly associated with the AGN (and thus effectively point-like at our resolution), for HIGs our results suggest that they are in general dominated by scattered light, a spatially resolved component. This is confirmed by several observations of imaging polarimetry and spectropolarimetry of radio-galaxies (e.g. Tadhunter et al. 2000; Ramirez et al. 2009). We then re-modeled the observed NIR brightness profiles taking into account the possibility that the central HIG sources are actually resolved and can be described by a gaussian light distribution. We considered in detail the three objects (3C 234[10], 3C 300, and 3C 349) that should have the larger scattered light fraction, being located closer to the grid origin in Fig. 10. For sizes larger than $\sim 0''.1$ significant residuals start to appear in the model fitting and we consider this value as an upper limit to the size of the scattering region. This corresponds to a range of 300-400 pc for these three objects, consistent with the size of the Seyfert polar scattering zone. This does not mean that there is no scattered light outside this region (as in e.g. 3C 321, Hurt et al. 1999), but it must be taken as an indication that the bulk of scattering occurs within this scale. The presence of low surface brightness scattered components (in contrast to the host galaxy) can only be probed with imaging polarimetry.

We conclude that HIG, unlike FR II LIGs, are consistent with the interpretation that they host a hidden quasar, but they are not simply partially obscured BLO. Scattered light must provide a substantial contribution to their nuclei in both the optical and NIR bands.

## 6. SUMMARY AND CONCLUSIONS

We have analyzed 1.6 $\mu$m near infrared images of 100 3CR radio galaxies from HST NICMOS in the F160W band with $z < 0.3$, $\sim$90% of the whole 3CR sample. On the basis of the radio morphology we divided the sample between FR I and FR II and from the point of view of their optical spectra we also classified them as Low Ionization Galaxies (LIG), High Ionization Galaxies (HIG), and Broad Line Objects (BLO).

We measured the nuclear NIR luminosity of all the objects, by subtracting the 1-D radial brightness profile (modeled with a Sérsic or core-Sérsic law representing the galaxy emission) from the total profile derived from the isophote fitting of the images.

The NIR nuclear emission is found to be strongly correlated with radio cores for FR Is. The linear correlation extends over $\sim$ 4 dex in luminosity with a rms of 0.4 dex and it has slope consistent with unity, as already found for the relations with optical and X-ray nuclei. This correlation provides further support to the identification of their nuclear emission as the synchrotron radiation produced in the inner part of the relativistic jet. In turn this implies a low contribution from thermal emission, an indication for the presence of radiatively inefficient disks. The similar dispersions for the correlations in NIR and in optical with the radio cores ascribes to the nuclear variability the dominant role of this scatter, rather than to obscuration.

[10] 3C 234 is a clear well-known case of optically obscured AGN with broad H$\alpha$ in polarized flux (Antonucci 1982, 1984; Young et al. 1998).

The large number of FR II LIGs present in this sample made possible for the first time a detailed analysis their nuclear properties in radio-infrared plane. We found a strong linear correlation between radio and NIR emission. The multiwavelength properties of FR II LIG nuclei are statistically indistinguishable from those of FR Is, indicating a common structure of the central engine, despite the difference in radio morphology and radio power. The similar nuclear properties suggest that the nuclei of FR II LIGs belong to the same class of those of FR Is, i.e., the nucleus is dominated by non-thermal emission from a relativistic jet.

All BLOs have detected NIR nuclei and show an NIR excess with respect to the FR I-FR II LIG radio-infrared correlation. This excess does not correlate with the radio cores, suggesting the presence of an additional infrared emitting component. In analogy with the properties of radio-quiet QSO, their optical nuclei most likely originate from the thermal emission of the accretion disk. Since their optical-infrared spectral indices are essentially flat, this suggests that thermal infrared emission from hot dust dominates in the NIR.

The origin of the NIR nuclei of HIGs is more complex. Although a few HIG nuclei lie on the FR I-FR II LIG radio-infrared correlation, most of them show a large NIR excess which does not correlate with the radio cores. This means that synchrotron emission from the jet base is not sufficient to explain their nuclear luminosities. Nonetheless, the HIG NIR nuclei are less luminous than those of BLOs, by a factor of 50 on average, suggesting partial obscuration, as expected by the unified model. Yet the infrared-optical luminosity ratios for HIGs are not consistent with a model of HIGs as the purely-obscured counterpart of the BLOs. We found that this inconsistency can be solved by including a significant contribution from nuclear light reflected in a compact circumnuclear scattering region. The sources which show the largest scattered light contribution, have a scatter region of 300-400 pc ($\sim 0\farcs1$).

The analysis of the properties of the NIR nuclear sources of 3CR radio-galaxies presented here broadly confirms the indications derived from the study of the optical nuclei. In particular, the presence of two classes of radio-loud AGN, LIG and HIG, with different nuclear properties is strengthened.

FR I radio-galaxies as well as the sub-population of sources with FR II morphology characterized by a low ionization optical spectrum belong to the same class from the nuclear point of view. In these sources the mechanism of emission related to the presence of non-thermal plasma from their radio-jets dominates over the contribution from thermal radiation related to the accretion process. Moving from optical to infrared observations has no substantial effect despite the reduced absorption at longer observing wavelengths. However the NIR band is not the optimal band to investigate the issue of obscuring tori. The data preseneted here leave the results based on optical observations unchanged, bearing in mind that for most of FR Is we have a clear view to their optical/infrared nucleus. While MIR Spitzer spectra (Leipski et al. 2009) obtained with a large slit size ($10.7''$) do show an infrared excess with respect to the jet emission in three FR I sources (and in one FR II LIG), our results on 3CR sample do not directly require the presence of dusty torus on the line of sight to the FR I nucleus. Furthermore, although Leipski et al. (2009) argue that the dust emission is powered the nucleus, the comparison between MIR spectra and HST data is extremely difficult because of the different spatial resolution of the two instruments. On the other hand, at this stage we cannot rule out the presence of a dusty torus in these objects because of the higher distance of the FR II LIGs than that of FR Is. Despite the lack of such information, the nuclear properties of FR II LIG nuclei are found to be statistically indistinguishable from those of FR Is. How all the sources of the FR I/FR II LIG group can be associated with such a large range of radio power, while still maintaining their disks in radiatively inefficient state, and what causes the transition to the FR II morphology in LIGs remain open questions.

The NIR data provide new insights also for the second class of objects, formed by HIGs and BLOs. The BLO NIR nuclei are likely to be dominated by the emission from hot dust located in the immediate vicinity of the active nucleus. In HIG we found many examples of nuclei in which the NIR emission is substantially larger than in the optical. Due to the proximity of the two bands, the only mechanism that can explain this effect is the presence of nuclear structures covered by absorbing material, optically thin at least in the infrared. Scattered light must provide a substantial contribution to their nuclei in both the optical and NIR bands. The lack of broad emission line in HIGs is universally associated with a substantially decreased luminosity of their nuclei in the infrared band and to a different angle of sight to the nucleus. This implies that obscuration still plays a substantial role.

The detailed comparison of radio, optical, and infrared data for the 3CR sample also shows that the differences in the relative contribution in these bands, on a object-by-object basis, is dominated by variability and not by absorption. Thus, only simultaneous nuclear data would allow us to explore intrinsic differences among the sources of the sample. The lack of such data effectively hampers the use of the nuclear Spectral Energy Distribution to enlighten how they vary with e.g., source power and viewing angle.

R.D.B. acknowledges the financial support (HST-GO-11219.07-A grant) from Space Telescope Science Institute, Baltimore. We are grateful to the referee, R. Antonucci for the extremely careful and detailed report which stimulated us and significantly contribuited to greatly improve the paper. We also thank G. K. Miley for useful comments.

## APPENDIX

It is interesting to investigate the radio and NIR correlation for FR Is by considering radio data of higher angular resolution. To this aim, we take from the literature the fluxes at 5 GHz obtained with VLBI observations. The FR Is for which the VLBI radio data are available are listed in Table 5. In Fig. 11 (left panel) we show the correlations in

TABLE 5
VLBI RADIO DATA

| name | $F_{VLBI}$ | $L_{VLBI}$ | Ref |
|---|---|---|---|
| 3C 31 | -24.04 | 29.69 | G05 |
| 3C 66 | -23.74 | 30.19 | G05 |
| 3C 83.1 | -24.57 | 29.50 | X99 |
| 3C 84 | -22.44 | 31.32 | K05 |
| 3C 264 | -23.70 | 30.20 | G05 |
| 3C 270 | -23.74 | 29.27 | J97 |
| 3C 272.1 | -23.74 | 28.67 | G05 |
| 3C 274 | -22.40 | 30.02 | G05 |
| 3C 296 | -24.19 | 29.83 | G05 |
| 3C 310 | -24.06 | 30.66 | G05 |
| 3C 317 | -23.53 | 30.80 | V00 |
| 3C 338 | -23.98 | 30.25 | G05 |
| 3C 346 | -23.66 | 31.95 | G05 |
| 3C 449 | -24.43 | 29.35 | G05 |
| 3C 465 | -23.61 | 30.61 | G05 |
| NGC 6251 | -23.44 | 30.61 | J86 |

NOTE. — Table of radio core flux and luminosity from VLBI observations. Col. (1): name; Col. (2): radio core flux in erg $s^{-1}$ $cm^{-2}$ $Hz^{-1}$; Col. (3): radio core luminosity in erg $s^{-1}$ $Hz^{-1}$; Col. (4): References:G05: Giovannini et al. (2005), X99: Xu et al. (1999b), K05: Kovalev et al. (2005) (VLBA at 15GHz), J97: Jones & Wehrle (1997) (VLBA at 1.6GHz), V00: Venturi et al. (2000), J86: Jones et al. (1986).

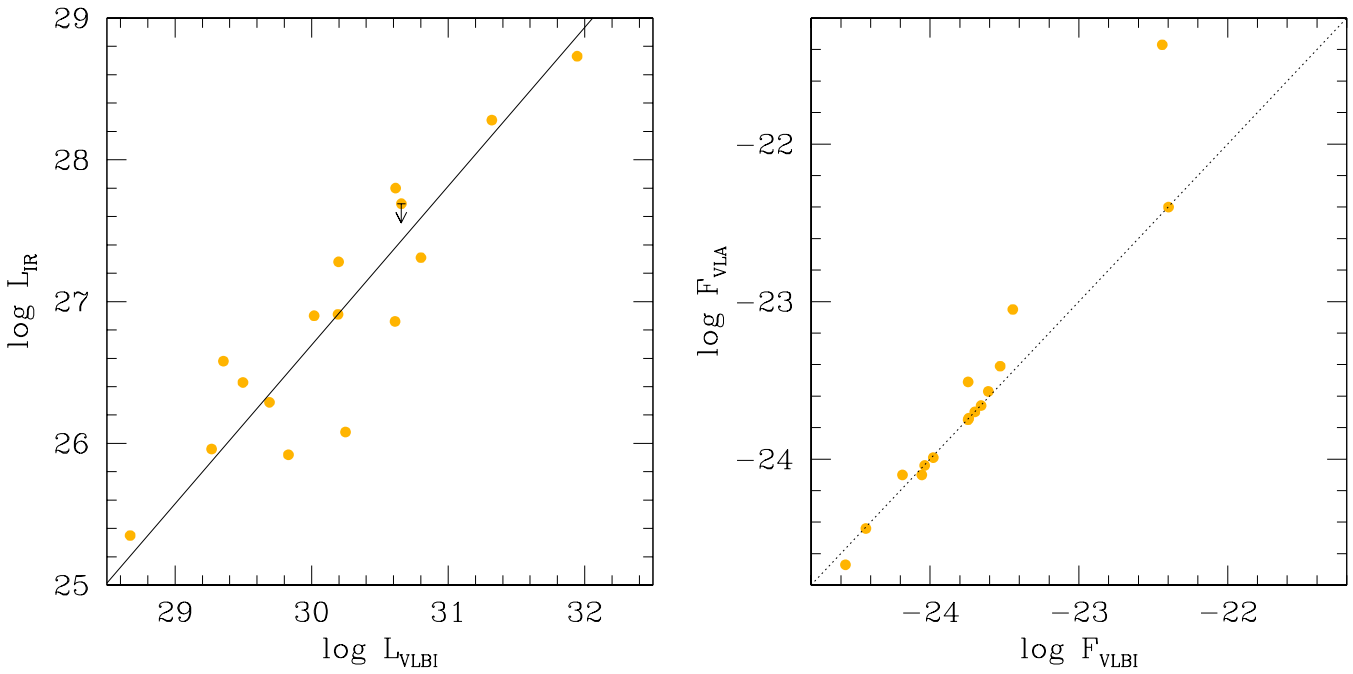


FIG. 11.— VLBI data. In left panel we compare the VLBI radio and HST NIR nuclear luminosities (in erg $s^{-1}$ $Hz^{-1}$) for the FR Is whose radio VLBI data are available. The solid lines represents the least-squared fits for the data shown in the plots. In right panel we compare the VLBI and VLA fluxes for the same FR I sub-sample. The dotted lines represents the bisectrix of the plane.

the $L_{VLBI}$-$L_{IR}$ planes. The linear correlation coefficient is r = 0.90 (P =$4.1\times10^{-6}$). These values as well as the slope and the intercept of the derived correlations are essentially identical to those obtained with the VLA data. The reason of these similarities can be explained by looking at Fig. 11 (right panel), which shows the VLA core flux of FR Is plotted vs. their VLBI flux. The figure clearly shows that the two measurements lead to very similar flux values. The dispersion is extremely small, with the exception of only two outliers (3C 84 and NGC 6251), for which the VLA flux is higher than that of VLBI by a factor of $\sim 2.5$ and $\sim 12$, respectively. However, since these two objects have a relatively high core dominance, they are likely to be observed at a small angle with respect to jet axis and thus they are more likely to be affected by flux variability. That might explain the larger discrepancy between the VLA and VLBI fluxes for these two sources with respect to the other FR Is. Summarizing, the correlation between the VLBI and the IR nuclear luminosity is statistically indistinguishable from that obtained using the VLA cores simply because

the core fluxes measured with VLA and VLBI are only marginally different.

REFERENCES


Akritas, M. 1989, Aligned Rank Tests for Regression With Censored Data (Penn State Dept. of Statistics Technical Report, 1989)
Akujor, C. E., & Garrington, S. T. 1995, A&AS, 112, 235
Allen, S. W., Dunn, R. J. H., Fabian, A. C., Taylor, G. B., & Reynolds, C. S. 2006, MNRAS, 372, 21
Antonucci, R. R. J. 1982, Nature, 299, 605
—. 1984, ApJ, 278, 499
—. 1986, ApJ, 304, 634
Antonucci, R. R. J., & Ulvestad, J. S. 1985, ApJ, 294, 158
Baggett, W. E., Baggett, S. M., & Anderson, K. S. J. 1998, AJ, 116, 1626
Baldi, R. D., & Capetti, A. 2008, A&A, 489, 989
Balmaverde, B., Baldi, R. D., & Capetti, A. 2008, A&A, 486, 119
Balmaverde, B., Capetti, A., & Grandi, P. 2006, A&A, 451, 35
Barthel, P. D. 1989, ApJ, 336, 606
Baum, S. A., & Heckman, T. 1989, ApJ, 336, 681
Baum, S. A., Zirbel, E. L., & O'Dea, C. P. 1995, ApJ, 451, 88
Bennett, A. S. 1962a, MNRAS, 125, 75
—. 1962b, MmRAS, 68, 163
Bicknell, G. V. 1984, ApJ, 286, 68
—. 1994, ApJ, 422, 542
Black, A. R. S., Baum, S. A., Leahy, J. P., Perley, R. A., Riley, J. M., & Scheuer, P. A. G. 1992, MNRAS, 256, 186
Buttiglione, S., Capetti, A., Celotti, A., Axon, D. J., Chiaberge, M., Macchetto, F. D., & Sparks, W. B. 2009, A&A, 495, 1033
—. 2010, A&A, 509, A6+
Byun, Y. I., & Freeman, K. C. 1995, ApJ, 448, 563
Caon, N., Capaccioli, M., & D'Onofrio, M. 1994, A&AS, 106, 199
Capaccioli, M. 1989, in World of Galaxies (Le Monde des Galaxies), ed. H. G. Corwin, Jr. & L. Bottinelli, 208–227
Capetti, A., Axon, D. J., Chiaberge, M., Sparks, W. B., Duccio Macchetto, F., Cracraft, M., & Celotti, A. 2007, A&A, 471, 137
Capetti, A., & Balmaverde, B. 2005, A&A, 440, 73
Capetti, A., Celotti, A., Chiaberge, M., de Ruiter, H. R., Fanti, R., Morganti, R., & Parma, P. 2002, A&A, 383, 104
Chakravarti, I. M., L. R. G., & Roy, J. 1967, Handbook of Methods of Applied Statistics, Vol. 1 (John Wiley and Sons), 392–394
Chiaberge, M. 2004, in Multiwavelength AGN Surveys, ed. R. Mújica & R. Maiolino, 217–+
Chiaberge, M., Capetti, A., & Celotti, A. 1999, A&A, 349, 77
—. 2000a, A&A, 355, 873
—. 2002a, A&A, 394, 791
Chiaberge, M., Celotti, A., Capetti, A., & Ghisellini, G. 2000b, A&A, 358, 104
Chiaberge, M., Macchetto, F. D., Sparks, W. B., Capetti, A., Allen, M. G., & Martel, A. R. 2002b, ApJ, 571, 247
Cleary, K., Lawrence, C. R., Marshall, J. A., Hao, L., & Meier, D. 2007, ApJ, 660, 117
Das, M., Vogel, S. N., Verdoes Kleijn, G. A., O'Dea, C. P., & Baum, S. A. 2005, ApJ, 629, 757
de Koff, S., Baum, S. A., Sparks, W. B., Biretta, J., Golombek, D., Macchetto, F., McCarthy, P., & Miley, G. K. 1996, ApJS, 107, 621
Dicken, D., Tadhunter, C., Axon, D., Morganti, R., Inskip, K. J., Holt, J., González Delgado, R., & Groves, B. 2009, ApJ, 694, 268
Donzelli, C. J., Chiaberge, M., Macchetto, F. D., Madrid, J. P., Capetti, A., & Marchesini, D. 2007, ApJ, 667, 780
Ekers, R. D., Fanti, R., & Miley, G. K. 1983, A&A, 120, 297
Elvis, M., Wilkes, B. J., McDowell, J. C., Green, R. F., Bechtold, J., Willner, S. P., Oey, M. S., Polomski, E., & Cutri, R. 1994, ApJS, 95, 1
Faber, S. M., Tremaine, S., Ajhar, E. A., Byun, Y., Dressler, A., Gebhardt, K., Grillmair, C., Kormendy, J., Lauer, T. R., & Richstone, D. 1997, AJ, 114, 1771
Fanaroff, B. L., & Riley, J. M. 1974, MNRAS, 167, 31P
Feigelson, E. D., & Nelson, P. I. 1985, ApJ, 293, 192
Fernini, I., Burns, J. O., & Perley, R. A. 1997, AJ, 114, 2292
Ferrarese, L., Côté, P., Jordán, A., Peng, E. W., Blakeslee, J. P., Piatek, S., Mei, S., Merritt, D., Milosavljević, M., Tonry, J. L., & West, M. J. 2006, ApJS, 164, 334
Floyd, D. J. E., Axon, D., Baum, S., Capetti, A., Chiaberge, M., Macchetto, D., Madrid, J., Miley, G., O'Dea, C. P., Perlman, E., Quillen, A., Sparks, W., & Tremblay, G. 2008, ApJS, 177, 148
Fomalont, E. B., & Bridle, A. H. 1978, AJ, 83, 725
Fossati, G., Maraschi, L., Celotti, A., Comastri, A., & Ghisellini, G. 1998, MNRAS, 299, 433
Ghisellini, G., Maraschi, L., & Treves, A. 1985, A&A, 146, 204
Giovannini, G., Feretti, L., Gregorini, L., & Parma, P. 1988, A&A, 199, 73
Giovannini, G., Taylor, G. B., Feretti, L., Cotton, W. D., Lara, L., & Venturi, T. 2005, ApJ, 618, 635
Gopal-Krishna, & Wiita, P. J. 2001, A&A, 373, 100
Graham, A. W., & Driver, S. P. 2005, Publications of the Astronomical Society of Australia, 22, 118
Haas, M., Müller, S. A. H., Bertoldi, F., Chini, R., Egner, S., Freudling, W., Klaas, U., Krause, O., Lemke, D., Meisenheimer, K., Siebenmorgen, R., & van Bemmel, I. 2004, A&A, 424, 531
Haas, M., Siebenmorgen, R., Schulz, B., Krügel, E., & Chini, R. 2005, A&A, 442, L39
Haas, M., Willner, S. P., Heymann, F., Ashby, M. L. N., Fazio, G. G., Wilkes, B. J., Chini, R., & Siebenmorgen, R. 2008, ApJ, 688, 122
Hardcastle, M. J. 1998, MNRAS, 298, 569
—. 1999, A&A, 349, 381
—. 2004, A&A, 414, 927
Hardcastle, M. J., Alexander, P., Pooley, G. G., & Riley, J. M. 1998, MNRAS, 296, 445
Hardcastle, M. J., Evans, D. A., & Croston, J. H. 2006, MNRAS, 370, 1893
Heraudeau, P., & Simien, F. 1996, A&AS, 118, 111
Hine, R. G., & Longair, M. S. 1979, MNRAS, 188, 111
Hine, R. G., & Scheuer, P. A. G. 1980, MNRAS, 193, 285
Hurt, T., Antonucci, R., Cohen, R., Kinney, A., & Krolik, J. 1999, ApJ, 514, 579
Isobe, T., Feigelson, E. D., Akritas, M. G., & Babu, G. J. 1990, ApJ, 364, 104
Isobe, T., Feigelson, E. D., & Nelson, P. I. 1986, ApJ, 306, 490
Jackson, C. A., & Wall, J. V. 1999, MNRAS, 304, 160
Jackson, N., & Rawlings, S. 1997, MNRAS, 286, 241
Jedrzejewski, R. I. 1987, MNRAS, 226, 747
Jones, D. L., Unwin, S. C., Readhead, A. C. S., Sargent, W. L. W., Seielstad, G. A., Simon, R. S., Walker, R. C., Benson, J. M., Perley, R. A., Bridle, A. H., Pauliny-Toth, I. I. K., Romney, J., Witzel, A., Wilkinson, P. N., Baath, L. B., Booth, R. S., Fort, D. N., Galt, J. A., Mutel, R. L., & Linfield, R. P. 1986, ApJ, 305, 684
Jones, D. L., & Wehrle, A. E. 1997, ApJ, 484, 186
Kaplan, E. L., & Meier, P. 1958, Nonparametric estimation from incomplete observations, Vol. 53 (J. Am. Stat. Assoc.), 457–481
Kendall, M. 1983, A New Measure of Rank Correlation, Vol. 30 (Biometrika), 81–89
Kharb, P., Lister, M. L., & Cooper, N. J. 2010, ApJ, 710, 764
Kovalev, Y. Y., Kellermann, K. I., Lister, M. L., Homan, D. C., Vermeulen, R. C., Cohen, M. H., Ros, E., Kadler, M., Lobanov, A. P., Zensus, J. A., Kardashev, N. S., Gurvits, L. I., Aller, M. F., & Aller, H. D. 2005, AJ, 130, 2473
Laing, R. A., Jenkins, C. R., Wall, J. V., & Unger, S. W. 1994, in The First Stromlo Symposium: The Physics of Active Galaxies. ASP Conference Series, Vol. 54, 1994, G.V. Bicknell, M.A. Dopita, and P.J. Quinn, Eds., p.201, 201–+
Landt, H., Bentz, M. C., Ward, M. J., Elvis, M., Peterson, B. M., Korista, K. T., & Karovska, M. 2008, ApJS, 174, 282
Lavalley, M., Isobe, T., & Feigelson, E. 1992, in Astronomical Society of the Pacific Conference Series, Vol. 25, Astronomical Data Analysis Software and Systems I, ed. D. M. Worrall, C. Biemesderfer, & J. Barnes, 245–+
Lawrence, C. R., Zucker, J. R., Readhead, A. C. S., Unwin, S. C., Pearson, T. J., & Xu, W. 1996, ApJS, 107, 541
Leahy, J. P., & Perley, R. A. 1991, AJ, 102, 537
Leipski, C., Antonucci, R., Ogle, P., & Whysong, D. 2009, ApJ, 701, 891
Madrid, J. P., Chiaberge, M., Floyd, D., Sparks, W. B., Macchetto, D., Miley, G. K., Axon, D., Capetti, A., O'Dea, C. P., Baum, S., Perlman, E., & Quillen, A. 2006, ApJS, 164, 307

Marchesini, D., Capetti, A., & Celotti, A. 2005, A&A, 433, 841
Marchesini, D., Celotti, A., & Ferrarese, L. 2004, MNRAS, 351, 733
Morganti, R., Killeen, N. E. B., & Tadhunter, C. N. 1993, MNRAS, 263, 1023
Netzer, H., Shemmer, O., Maiolino, R., Oliva, E., Croom, S., Corbett, E., & di Fabrizio, L. 2004, ApJ, 614, 558
Nilsson, K. 1998, A&AS, 132, 31
Ogle, P., Whysong, D., & Antonucci, R. 2006, ApJ, 647, 161
Okuda, T., Kohno, K., Iguchi, S., & Nakanishi, K. 2005, ApJ, 620, 673
Osterbrock, D. E. 1989, Astrophysics of gaseous nebulae and active galactic nuclei (Research supported by the University of California, John Simon Guggenheim Memorial Foundation, University of Minnesota, et al. Mill Valley, CA, University Science Books, 1989, 422 p.)
Osterbrock, D. E., & Miller, J. S. 1975, ApJ, 197, 535
Owen, F. N., & Laing, R. A. 1989, MNRAS, 238, 357
Owen, F. N., Ledlow, M. J., & Keel, W. C. 1996, AJ, 111, 53
Pearson, T. J., & Readhead, A. C. S. 1981, ApJ, 248, 61
Peng, C. Y., Ho, L. C., Impey, C. D., & Rix, H.-W. 2002, AJ, 124, 266
Perley, R. A., Bridle, A. H., & Willis, A. G. 1984, ApJS, 54, 291
Perlman, E. S., Harris, D. E., Biretta, J. A., Sparks, W. B., & Macchetto, F. D. 2003, ApJ, 599, L65
Peto, R., & Peto, J. 1972, Asymptotically efficient rank invariant procedures, Vol. 135 (Journal of the Royal Statistical Society), 185–207
Phillips, M. M., & Osterbrock, D. E. 1975, PASP, 87, 949
Ramirez, E. A., Tadhunter, C. N., Axon, D., Batcheldor, D., Young, S., Packham, C., & Sparks, W. B. 2009, ArXiv e-prints
Rawlings, S., & Saunders, R. 1991, Nature, 349, 138
Rawlings, S., Saunders, R., Eales, S. A., & Mackay, C. D. 1989, MNRAS, 240, 701
Riffel, R., Rodríguez-Ardila, A., & Pastoriza, M. G. 2006, A&A, 457, 61
Riley, J. M., & Pooley, G. G. 1975, MmRAS, 80, 105
Schmitt, J. H. M. M. 1985, ApJ, 293, 178
Sersic, J. L. 1968, Atlas de galaxias australes (Cordoba, Argentina: Observatorio Astronomico, 1968)
Shi, Y., Rieke, G. H., Hines, D. C., Neugebauer, G., Blaylock, M., Rigby, J., Egami, E., Gordon, K. D., & Alonso-Herrero, A. 2005, ApJ, 629, 88
Shuder, J. M., & Osterbrock, D. E. 1981, ApJ, 250, 55
Siebenmorgen, R., Freudling, W., Krügel, E., & Haas, M. 2004, A&A, 421, 129
Smolčić, V. 2009, ApJ, 699, L43
Spangler, S. R., Myers, S. T., & Pogge, J. J. 1984, AJ, 89, 1478
Spangler, S. R., & Sakurai, T. 1985, ApJ, 297, 84
Spencer, R. E., Schilizzi, R. T., Fanti, C., Fanti, R., Parma, P., van Breugel, W. J. M., Venturi, T., Muxlow, T. W. B., & Rendong, N. 1991, MNRAS, 250, 225
Spinrad, H., Marr, J., Aguilar, L., & Djorgovski, S. 1985, PASP, 97, 932
Tadhunter, C. N., Sparks, W., Axon, D. J., Bergeron, L., Jackson, N. J., Packham, C., Hough, J. H., Robinson, A., & Young, S. 2000, MNRAS, 313, L52
Taylor, G. B., Vermeulen, R. C., Readhead, A. C. S., Pearson, T. J., Henstock, D. R., & Wilkinson, P. N. 1996, ApJS, 107, 37
Trujillo, I., Erwin, P., Asensio Ramos, A., & Graham, A. W. 2004, AJ, 127, 1917
Trussoni, E., Capetti, A., Celotti, A., Chiaberge, M., & Feretti, L. 2003, A&A, 403, 889
Tsvetanov, Z. I., Hartig, G. F., Ford, H. C., Dopita, M. A., Kriss, G. A., Pei, Y. C., Dressel, L. L., & Harms, R. J. 1998, ApJ, 493, L83+
Urry, C. M., & Padovani, P. 1995, PASP, 107, 803
van Breugel, W., & Jagers, W. 1982, A&AS, 49, 529
van der Wolk, G., Barthel, P. D., Peletier, R. F., & Pel, J. W. 2009, ArXiv e-prints
Venturi, T., Morganti, R., Tzioumis, T., & Reynolds, J. 2000, A&A, 363, 84
Verdoes Kleijn, G. A., Baum, S. A., de Zeeuw, P. T., & O'Dea, C. P. 2002, AJ, 123, 1334
Vermeulen, R. C., Ogle, P. M., Tran, H. D., Browne, I. W. A., Cohen, M. H., Readhead, A. C. S., Taylor, G. B., & Goodrich, R. W. 1995, ApJ, 452, L5+
Waggett, P. C., Warner, P. J., & Baldwin, J. E. 1977, MNRAS, 181, 465
Walker, R. C., Benson, J. M., Unwin, S. C., Lystrup, M. B., Hunter, T. R., Pilbratt, G., & Hardee, P. E. 2001, ApJ, 556, 756
Wall, J. V., & Jackson, C. A. 1997, MNRAS, 290, L17
Whysong, D., & Antonucci, R. 2004, ApJ, 602, 116
Wilcoxon, F. 1945, Individual comparisons by ranking methods. Biometrics, Vol. 1, 80–83
Xu, C., Livio, M., & Baum, S. 1999a, AJ, 118, 1169
Xu, C., O'Dea, C. P., & Biretta, J. A. 1999b, AJ, 117, 2626
Young, S., Hough, J. H., Axon, D. J., Fabian, A. C., & Ward, M. J. 1998, MNRAS, 294, 478
Zirbel, E. L. 1997, ApJ, 476, 489
Zirbel, E. L., & Baum, S. A. 1995, ApJ, 448, 521